REPORT DOCUMENTATION PAGE

Form Approved OMB NO. 0704-0188

1. REPORT DATE (DD-MM-YYYY)	2. REPORT TYPE	3. DATES COVERED (From - To)
10-08-2015	Book Chapter	-

4. TITLE AND SUBTITLE
Multiscale Modeling of Porouse Medium Systems

5a. CONTRACT NUMBER
W911NF-14-1-0287

5b. GRANT NUMBER

5c. PROGRAM ELEMENT NUMBER
611102

6. AUTHORS
J.E. McClure, W.G. Gray, C.T. Miller, A.L. Dye

5d. PROJECT NUMBER

5e. TASK NUMBER

5f. WORK UNIT NUMBER

7. PERFORMING ORGANIZATION NAMES AND ADDRESSES
University of North Carolina - Chapel Hill
104 Airport Drive, CB 1350
Suite 2200
Chapel Hill, NC 27599 -1350

8. PERFORMING ORGANIZATION REPORT NUMBER

9. SPONSORING/MONITORING AGENCY NAME(S) AND ADDRESS (ES)
U.S. Army Research Office
P.O. Box 12211
Research Triangle Park, NC 27709-2211

10. SPONSOR/MONITOR'S ACRONYM(S)
ARO

11. SPONSOR/MONITOR'S REPORT NUMBER(S)
65276-MA.3

12. DISTRIBUTION AVAILIBILITY STATEMENT
Approved for public release; distribution is unlimited.

13. SUPPLEMENTARY NOTES
The views, opinions and/or findings contained in this report are those of the author(s) and should not contrued as an official Department of the Army position, policy or decision, unless so designated by other documentation.

14. ABSTRACT
The thermodynamically constrained averaging theory is used to formulate a model to describe two-fluid-phase flow in a porous medium system. Microfluidic experiments and lattice-Boltzmann modeling are used to examine the closure relations needed to form a closed well-posed model. Comparisons are made with other model formulations approaches and the advantages of the TCAT model are listed. The challengs remaining are discussed.

15. SUBJECT TERMS
TCAT, Model formulation, Two-fluid-phase flow

16. SECURITY CLASSIFICATION OF:			17. LIMITATION OF ABSTRACT	15. NUMBER OF PAGES	19a. NAME OF RESPONSIBLE PERSON
a. REPORT	b. ABSTRACT	c. THIS PAGE			Cass Miller
UU	UU	UU	UU		19b. TELEPHONE NUMBER 919-966-2643

Report Title

Multiscale Modeling of Porouse Medium Systems

ABSTRACT

The thermodynamically constrained averaging theory is used to formulate a model to describe two-fluid-phase flow in a porous medium system. Microfluidic experiments and lattice-Boltzmann modeling are used to examine the closure relations needed to form a closed well-posed model. Comparisons are made with other model formulations approaches and the advantages of the TCAT model are listed. The challengs remaining are discussed.

1 Multiscale Modeling of Porous Medium Systems

Amanda L. Dye, James E. McClure, William G. Gray, and Cass T. Miller

CONTENTS

1.1 INTRODUCTION

The use of computers over the last 60 years for simulating subsurface flow problems has provided an impressive, ever-expanding ability to model processes at a high resolution. Whereas in the 1960s a computational grid with 500 fixed nodes would have pushed the boundaries of computer power [59], simulations today involve millions of spatial grid points and adaptive meshes [40,57]. The availability of this power for solving equations that purport to describe physical and chemical processes in porous media is wasted, however, if the equations being used to describe

the systems are inadequate. Most assuredly, the ability to solve equations that are posed has been vastly improved. Unfortunately, the equations that are being solved have not developed to the same degree.

For example, the primary equation for describing momentum transport of fluids in porous media is Darcy's law, a correlation of data from a highly idealized set of experiments (e.g., homogeneous medium, single-fluid phase, steady state) published in 1856 [9,16,17]. The results of these experiments have been presumed to apply to transient, multiphase flows in heterogeneous systems at different scales. This extension of the experiment to systems clearly beyond their scope has resulted in equations with ill-defined and poorly understood variables. A clear path for rigorously extending the form of Darcy's equation to flows well beyond those considered by Darcy, such as high-velocity flow and flows with cross coupling between the fluid phases, does not exist. Furthermore, inclusion of physical phenomena such as capillary pressure, contact angles, and evolution of interfaces between phases has been a heuristic effort justified somewhat by dabbling in physical understanding rather than a comprehensive rigorous derivation of equations that describe the processes (e.g., [34,49,53]).

Averaging of equations from the microscale to a larger scale is one general approach that has been employed in an effort to obtain equations that have a firm theoretical basis. Underlying averaging theory is the mathematical theorems that allow transformation of the scale of equations. Theorems for transformation of conservation equations for phases have been employed for almost 50 years [3,4,60,68]. Theorems that allow averaging of equations for interfaces between phases and for common curves, where three interfaces meet, were developed subsequently [22,30], and the forms of all these equations have been unified [27]. Four principal variants of averaging theory that make use of these theorems have been employed. The first emphasizes averaging of microscale conservation equations for phases and then makes heuristic arguments to close the equation system (e.g., [6,29,68]).

A second approach pioneered by Whitaker, and employed by adherents to this approach, is commonly referred to as the method of volume averaging (MVA). Applications of MVA typically make use of averaging theorems applied to conservation equations for phases only. This approach begins with closed microscale equations, which are then averaged to a larger scale. The new terms that arise are closed typically by derivation of closure equations solved for a periodic unit cell and the solution of closure variables to map from the smaller scale to the larger scale (e.g., [8,15,21,54–56,61,69,71]).

The third approach makes use of averaging of conservation equations in conjunction with rational thermodynamics (ACRT). ACRT averages equations for phases, interfaces, and common curves. Then, based on a set of axioms concerning system behavior, thermodynamic relations are obtained directly at the larger scale; and the equation set is closed based on exploitation of an entropy inequality (e.g., [7,31,33,64]).

These preceding methods have shortcomings primarily in that the first two methods do not account for interface dynamics and require assumptions about the forms for deviations between microscale and larger-scale values. The approaches make very limited use of thermodynamic information. ACRT suffers in that the larger-scale thermodynamic relations in fact are expressed in terms of quantities that are not based on fundamental thermodynamic variables [5,42,44,66]. Additionally, these models have been abused by using erroneous closure conditions for the interface stress tensor and the interface dynamics (e.g., [50,51]). Thus, complete and correct models based on averaged conservation equations, thermodynamics, and phase distribution kinematics are missing.

In an effort to overcome the problems of these earlier methods, a fourth method, referred to as thermodynamically constrained averaging theory (TCAT), has been formulated. This method is the basis of this contribution. Here, we outline the elements of TCAT and show how it can be used to obtain model equations that overcome many theoretical difficulties.

1.2 OVERVIEW

Conservation equations and thermodynamic relations applicable to porous medium systems are well understood at the microscale where the boundaries between all phases are resolved and evolved dynamically. However, many porous medium systems are described at a scale above the microscale, where a point refers to the averaged conditions in some representative averaging region. We will call this larger scale the macroscale. The TCAT has been developed to formulate macroscale models such that all variables are expressed explicitly in terms of microscale precursors [24,28]. TCAT also assures consistency with the second law of thermodynamics. It has been shown that use of the TCAT procedure leads to the occurrence of variables such as volume fractions, interfacial tensions, and density of interfacial area between the fluid and solid phases for the case of single-fluid porous medium systems. For multifluid systems, common curve lengths per volume, interfacial tensions, curvatures, and contact angles also arise naturally in the formulation [39]. On physical grounds, these variables can be argued to be of importance; their magnitudes relate to possibilities for interactions and exchanges between phases. However, these variables do not appear explicitly in traditional porous medium models.

Despite the theoretical appeal of TCAT models, a problem remains; solvable models require the explicit identification of closure relations that have only been specified in general functional forms by the theoretical work advanced to date. The constitutive relations employed for a particular system must be consistent with the general functional dependences inferred and must also be clearly stipulated and parameterized. Closed models are needed both to facilitate solution of an equation set and to allow for validation of TCAT models by comparison with system behavior observed at the corresponding scale.

In recent years, some needed closed forms have been motivated by small-scale experimental and computational methods. Of particular interest here is the high-resolution microscale modeling approach known as the lattice Boltzmann method (LBM). This method can be used to generate both a detailed understanding of microscale transport phenomena within the pores of a porous medium system and also the macroscale variables that can be obtained as integrated forms of the microscale variables. These macroscale variables can be employed in posited general forms of closure relations [20,32,52,65]. Computational experiments thus provide a basis for the development of closed models making use of equations developed using the TCAT procedure. Because TCAT models are new, multiscale modeling of specific forms of TCAT closure relations has not yet been completed for many theorized model formulations.

In this chapter, we examine a TCAT model for two-fluid-phase flow in a porous medium system. In Section 1.3, we provide the theoretical elements that are combined to establish the TCAT approach. In Section 1.4 we propose a set of closed equations that describes two-fluid-phase flow in a porous medium. For this set to be solvable, values or functional forms of some coefficients and equations of state must be specified. In Section 1.5, we discuss how knowledge of the smaller-scale system behavior, obtained through complementary experimental and LBM studies, can provide insights for specification of the needed forms and coefficients. Section 1.6 provides details concerning the formulation, verification, and validation of the LBM approach used to simulate two-fluid-phase flow in a porous medium system. The resultant model is used to investigate various aspects of the flow system that the TCAT model suggests warrant attention, such as an appropriate formulation of capillary pressure. The need to obtain information about geometric features of the porous medium system, such as the curvature of interfaces between phases and the extent of those interfaces, is discussed in Section 1.7. In Section 1.8, specific closure relations for a two-fluid-phase system are obtained from analysis of LBM simulations. This serves as an illustration of how robust models and formulations can be advanced by rigorous theoretical analysis in conjunction with computer simulation for a range of phenomena.

1.3 THEORY

TCAT is a systematic procedure for changing the scale of conservation, balance, and thermodynamic equations from the microscale to a larger scale. For use in porous media, the TCAT method involves averaging over a representative averaging volume to obtain equations for phases, interfaces between phases, common curves, and common points, which are referred to generically as entities. TCAT has been developed by considering each of these entities separately. Here, we will make use of the similarities of the equations and averaging theorems for each of the different entity types to develop the equations. The following six sections present the essential TCAT components: averaging theorems, conservation equations, entropy balance, thermodynamic equations, evolution equations, and the entropy inequality. The full details of these equations and the procedures used to manipulate them can be found in [28]. Here, we emphasize the equations that are particularly useful in macroscale porous medium flow modeling. These results form the bases for model formulation and closure considerations, which are considered subsequently.

1.3.1 Averaging Theorems

For porous medium analysis, it is not possible to model large systems at a microscale where the flow profile within the pores is described. Neither is it always informative to model the system at a megascale where only an average value of a quantity within the full system is determined. As a compromise between these two extremes, it is important to be able to model natural systems and laboratory systems at an intermediate length scale, referred to as the macroscale, where a filtered form of quantities in the system is used. At the microscale, the phases within a system are visualized as being juxtaposed and separated by interfaces. At a microscale location, a point lies within a single phase or on an interface or a common curve. From a macroscale perspective, all phases, interfaces, and common curves may be present at a location with each having a geometric density. A phase has a volume fraction measure, an interface has an interfacial area per volume measure, and a common curve has a length per volume measure. A similar density can be developed for common points, which do not occur in the systems considered in this chapter.

The conservation and balance equations that describe a system are most easily formulated directly in terms of microscale quantities. To transform the microscale equations to the macroscale, mathematical relations are needed. These have the effect of changing averages of derivatives of microscale quantities into derivatives of macroscale quantities. These theorems [3,22,23,27,30,37,43,47,60,67] are most readily applied when the length scales of the microscale and macroscale are widely separated. Microscale phase conservation equations are 3D transient forms. Interface conservation equations are 2D at the microscale. Common curves and common points are, respectively, one and zero dimensional at the microscale. On transformation to the macroscale, all these equations become 3D as the properties of interest vary in space regardless of the type of entity to which they belong.

The spatial averaging theorems are applied, respectively, to the divergence and gradient operators according to

$$\left\langle \nabla^{(n)} \cdot \mathbf{f}_\alpha \right\rangle_{\Omega_\alpha,\Omega} = \nabla \cdot \left\langle \mathbf{l}_\alpha^{(n)} \cdot \mathbf{f}_\alpha \right\rangle_{\Omega_\alpha,\Omega} - \left\langle \left(\nabla^{(n)} \cdot \mathbf{l}_\alpha^{(n)} \right) \cdot \mathbf{f}_\alpha \right\rangle_{\Omega_\alpha,\Omega} + \sum_{\kappa \in \mathcal{J}_{c\alpha}} \left\langle \mathbf{n}_\alpha \cdot \mathbf{f}_\alpha \right\rangle_{\Omega_\kappa,\Omega} \tag{1.1}$$

and

$$\left\langle \nabla^{(n)} f_\alpha \right\rangle_{\Omega_\alpha,\Omega} = \nabla \cdot \left\langle \mathbf{l}_\alpha^{(n)} f_\alpha \right\rangle_{\Omega_\alpha,\Omega} - \left\langle \left(\nabla^{(n)} \cdot \mathbf{l}_\alpha^{(n)} \right) f_\alpha \right\rangle_{\Omega_\alpha,\Omega} + \sum_{\kappa \in \mathcal{J}_{c\alpha}} \left\langle \mathbf{n}_\alpha f_\alpha \right\rangle_{\Omega_\kappa,\Omega}, \tag{1.2}$$

where (n) is the number of primes that appears in the superscript, the integration domain is of dimensionality $3 - n$, and the averaging operator is indicated using angle brackets. Thus, for example, for a surface of dimensionality 2, (n) = (1), so the microscale surface gradient operator, ∇', uses a single $'$ to indicate that it is a surface operator. For a phase, $n = 0$ and $\mathbf{l}_\alpha^{(0)} = \mathbf{l}$. For a common point, $n = 3$ and $\mathbf{l}_\alpha^{(3)} = \mathbf{0}$. Note that all variables and operators are defined in the nomenclature section.

In addition to the spatial averaging theorems, a temporal averaging theorem is employed that relates the spatial average of a time derivative of a function to the time derivative of the spatial average of the function. This theorem is stated

$$\left\langle \frac{\partial^{(n)} f_\alpha}{\partial t} \right\rangle_{\Omega_\alpha,\Omega} = \frac{\partial}{\partial t}\left\langle f_\alpha \right\rangle_{\Omega_\alpha,\Omega} + \nabla\cdot\left\langle \left(\mathbf{l} - \mathbf{l}_\alpha^{(n)}\right)\right\rangle\cdot \mathbf{v}_\alpha f_\alpha \Big\rangle_{\Omega_\alpha,\Omega} + \left\langle \nabla^{(n)}\cdot \mathbf{l}_\alpha^{(n)}\cdot \mathbf{v}_\alpha f_\alpha \right\rangle_{\Omega_\alpha,\Omega} - \sum_{\kappa\in\mathcal{J}_{c\alpha}^-} \left\langle \mathbf{n}_\alpha\cdot\mathbf{v}_\kappa f_\alpha \right\rangle_{\Omega_\kappa,\Omega}, \tag{1.3}$$

where

(n) is the number of primes that appears in the superscript
the integration domain, Ω_α, is of dimensionality $3 - n$

Equations 1.1 and 1.3 are the primary averaging theorems that are used to convert microscale conservation equations for phases, interfaces, common curves, and common points to their macroscale forms.

1.3.2 Conservation and Balance Equations

The conservation equations at the macroscale can all be derived from the microscale total energy equation by application of the averaging theorems followed by the restriction that the equation obtained must apply in any inertial coordinate system. In the development here, we will not consider species transport or interphase mass transfer of individual species. We state the microscale total energy equation for entity α as

$$\begin{aligned}\mathcal{E}_\alpha :=& \frac{\partial^{(n)}}{\partial t}\left(E_\alpha + \rho_\alpha \frac{\mathbf{v}_\alpha\cdot\mathbf{v}_\alpha}{2} + \Psi_\alpha\right) + \nabla^{(n)}\cdot\left[\left(E_\alpha + \rho_\alpha \frac{\mathbf{v}_\alpha\cdot\mathbf{v}_\alpha}{2} + \Psi_\alpha\right)\mathbf{v}_\alpha\right] \\ & - h_\alpha - \rho_\alpha \frac{\partial^{(n)}\psi_\alpha}{\partial t} - \rho_\alpha \mathbf{g}_\alpha\cdot\left(\mathbf{l} - \mathbf{l}_\alpha^{(n)}\right)\cdot\mathbf{v}_\alpha \\ & - \sum_{\kappa\in\mathcal{J}_{c\alpha}^+}\left[\left(\frac{E_\kappa}{\rho_\kappa} + \frac{\mathbf{v}_\kappa\cdot\mathbf{v}_\kappa}{2} + \psi_\kappa\right)\underset{\kappa\to\alpha}{M} + \mathbf{v}_\kappa\cdot\underset{\kappa\to\alpha}{\mathbf{T}} + \underset{\kappa\to\alpha}{Q}\right] \\ & - \nabla^{(n)}\cdot\left(\mathbf{l}_\alpha^{(n)}\cdot\mathbf{t}_\alpha\cdot\mathbf{v}_\alpha + \mathbf{l}_\alpha^{(n)}\cdot\mathbf{q}_\alpha\right) = 0 \quad \text{for } \alpha\in\mathcal{J}; n = 3 - \dim\alpha,\end{aligned} \tag{1.4}$$

where the summation term in this equation accounts for exchanges with entities of higher dimensionality.

This equation is averaged to the macroscale using the operator $\langle\cdot\rangle_{\Omega_\alpha,\Omega}$. After application of the averaging theorems Equations 1.1 and 1.3, the macroscale energy equation that results is

$$\begin{aligned}
\mathcal{E}^{\bar{\bar{\alpha}}} :=& \frac{\partial}{\partial t}\left[E^{\bar{\bar{\alpha}}} + \epsilon^{\bar{\bar{\alpha}}}\rho^{\bar{\alpha}}\left(\frac{\mathbf{v}^{\bar{\alpha}}\cdot\mathbf{v}^{\bar{\alpha}}}{2} + K_E^{\bar{\bar{\alpha}}}\right) + \Psi^{\bar{\bar{\alpha}}}\right] \\
&+ \nabla\cdot\left\{\left[E^{\bar{\bar{\alpha}}} + \epsilon^{\bar{\bar{\alpha}}}\rho^{\alpha}\left(\frac{\mathbf{v}^{\bar{\alpha}}\cdot\mathbf{v}^{\bar{\alpha}}}{2} + K_E^{\bar{\bar{\alpha}}}\right) + \Psi^{\bar{\bar{\alpha}}}\right]\mathbf{v}^{\bar{\alpha}}\right\} \\
&- \epsilon^{\bar{\bar{\alpha}}}h^{\alpha} - \sum_{\kappa\in\mathcal{J}_{c\alpha}}^{\kappa\to\alpha} M\left(\bar{\bar{E}}^{\bar{\bar{\alpha},\kappa}} + \frac{\mathbf{v}^{\bar{\bar{\alpha},\kappa}}\cdot\mathbf{v}^{\bar{\bar{\alpha},\kappa}}}{2} + K_E^{\bar{\bar{\alpha},\kappa}} + \psi^{\bar{\bar{\alpha},\kappa}}\right) \\
&- \sum_{\kappa\in\mathcal{J}_{c\alpha}}^{\kappa\to\alpha} \mathbf{T}\cdot\mathbf{v}^{\bar{\bar{\alpha},\kappa}} - \sum_{\kappa\in\mathcal{J}_{c\alpha}}^{\kappa\to\alpha} Q \\
&- \nabla\cdot\left(\epsilon^{\bar{\bar{\alpha}}}\mathbf{t}^{\bar{\bar{\alpha}}}\cdot\mathbf{v}^{\bar{\alpha}} + \epsilon^{\bar{\bar{\alpha}}}\mathbf{q}^{\bar{\bar{\alpha}}} + \epsilon^{\bar{\bar{\alpha}}}\mathbf{q}_{\mathrm{g}}^{\bar{\bar{\alpha}}}\right) - \left\langle\rho_\alpha\frac{\partial^{(n)}\psi_\alpha}{\partial t}\right\rangle_{\Omega_\alpha,\Omega} \\
&- \left\langle\rho_\alpha\mathbf{v}_\alpha\cdot\left(\mathbf{l} - \mathbf{l}_\alpha^{(n)}\right)\cdot\mathbf{g}_\alpha\right\rangle_{\Omega_\alpha,\Omega} = 0 \quad \text{for}\,\alpha\in\mathcal{J}; n = 3 - \dim\alpha.
\end{aligned} \tag{1.5}$$

The notation used in this equation is designed to precisely indicate the macroscale quantities (with superscripts), particular kinds of averages (spatial average with no overbar on the superscript, mass density weighted with a single overbar on the superscript, specially defined with a double overbar on the superscript), and an exchange term between entities (with a super arrow indicating the transfer from one entity to the other). The definitions arise naturally in the averaging process, and the expressions in terms of microscale variables appear in the nomenclature or in far greater detail in [28]. It is useful to rewrite the first two terms in Equation 1.5 making use of the material derivative operator to obtain

$$\begin{aligned}
\mathcal{E}_*^{\bar{\bar{\alpha}}} :=& \frac{\mathrm{D}^{\bar{\alpha}}}{\mathrm{D}t}\left[E^{\bar{\bar{\alpha}}} + \epsilon^{\bar{\bar{\alpha}}}\rho^{\alpha}\left(\frac{\mathbf{v}^{\bar{\alpha}}\cdot\mathbf{v}^{\bar{\alpha}}}{2} + K_E^{\bar{\bar{\alpha}}}\right) + \Psi^{\bar{\bar{\alpha}}}\right] \\
&+ \left[E^{\bar{\bar{\alpha}}} + \epsilon^{\bar{\bar{\alpha}}}\rho^{\alpha}\left(\frac{\mathbf{v}^{\bar{\alpha}}\cdot\mathbf{v}^{\bar{\alpha}}}{2} + \boldsymbol{K}_E^{\bar{\bar{\alpha}}}\right) + \Psi^{\bar{\bar{\alpha}}}\right]\mathbf{I}:\mathbf{d}^{\bar{\bar{\alpha}}} \\
&- \epsilon^{\bar{\bar{\alpha}}}h^{\alpha} - \sum_{\kappa\in\mathcal{J}_{c\alpha}}^{\kappa\to\alpha} M\left(\bar{\bar{E}}^{\bar{\bar{\alpha},\kappa}} + \frac{\mathbf{v}^{\bar{\bar{\alpha},\kappa}}\cdot\mathbf{v}^{\bar{\bar{\alpha},\kappa}}}{2} + K_E^{\bar{\bar{\alpha},\kappa}} + \psi^{\bar{\bar{\alpha},\kappa}}\right) \\
&- \sum_{\kappa\in\mathcal{J}_{c\alpha}}^{\kappa\to\alpha} \mathbf{T}\cdot\mathbf{v}^{\bar{\bar{\alpha},\kappa}} - \sum_{\kappa\in\mathcal{J}_{c\alpha}}^{\kappa\to\alpha} Q \\
&- \nabla\cdot\left(\epsilon^{\bar{\bar{\alpha}}}\mathbf{t}^{\bar{\bar{\alpha}}}\cdot\mathbf{v}^{\bar{\alpha}} + \epsilon^{\bar{\bar{\alpha}}}\mathbf{q}^{\bar{\bar{\alpha}}} + \epsilon^{\bar{\bar{\alpha}}}\mathbf{q}_{\mathrm{g}}^{\bar{\bar{\alpha}}}\right) - \left\langle\rho_\alpha\frac{\partial^{(n)}\psi_\alpha}{\partial t}\right\rangle_{\Omega_\alpha,\Omega} \\
&- \left\langle\rho_\alpha\mathbf{v}_\alpha\cdot\left(\mathbf{l} - \mathbf{l}_\alpha^{(n)}\right)\cdot\mathbf{g}_\alpha\right\rangle_{\Omega_\alpha,\Omega} = 0 \quad \text{for}\,\alpha\in\mathcal{J}; n = 3 - \dim\alpha.
\end{aligned} \tag{1.6}$$

This energy equation must apply in any inertial reference coordinate system. We can replace $\mathbf{v}^{\bar{\alpha}}$ by $\mathbf{v}^{\bar{\alpha}} + \mathbf{C}$, where $\mathbf{C}$ is an arbitrary constant velocity vector, and Equation 1.6 will still apply. After making this substitution, collection of terms that multiply $\mathbf{C}$ results in an equation of the form

$$\boldsymbol{\mathcal{E}}_*^{\bar{\bar{\alpha}}} + \mathbf{C} \cdot \boldsymbol{\mathcal{P}}_*^{\bar{\bar{\alpha}}} + \frac{\mathbf{C} \cdot \mathbf{C}}{2} \boldsymbol{\mathcal{M}}_*^{\bar{\bar{\alpha}}} = 0. \tag{1.7}$$

Because $\mathbf{C}$ is arbitrary, selection of $\mathbf{C} = \mathbf{0}$ confirms that Equation 1.6 still applies. If $\mathbf{C}$ is orthogonal to the terms collected to form $\boldsymbol{\mathcal{P}}_*^{\bar{\bar{\alpha}}}$, then Equation 1.7 requires that $\mathcal{M}_*^{\bar{\bar{\alpha}}} = 0$. Therefore, we must also have $\boldsymbol{\mathcal{P}}_*^{\bar{\bar{\alpha}}} = \mathbf{0}$, since Equation 1.7 must hold for any and all constant $\mathbf{C}$. The group of terms that comprises $\boldsymbol{\mathcal{P}}_*^{\bar{\bar{\alpha}}}$ is the momentum equation as follows:

$$\begin{aligned} \boldsymbol{\mathcal{P}}_*^{\bar{\bar{\alpha}}} := & \frac{\mathrm{D}^{\bar{\alpha}}}{\mathrm{D}t}\left(\epsilon^{\bar{\bar{\alpha}}} \rho^{\alpha} \mathbf{v}^{\bar{\alpha}}\right) + \epsilon^{\bar{\bar{\alpha}}} \rho^{\alpha} \mathbf{v}^{\bar{\alpha}} \mathbf{I} : \mathbf{d}^{\bar{\bar{\alpha}}} - \epsilon^{\bar{\bar{\alpha}}} \rho^{\alpha} \mathbf{g}^{\bar{\alpha}} \\ & - \sum_{\kappa \in \mathcal{J}_{c\alpha}} {}^{\kappa \to \alpha}M \, \overline{\overline{\mathbf{v}^{\alpha,\kappa}}} - \sum_{\kappa \in \mathcal{J}_{c\alpha}} {}^{\kappa \to \alpha}\mathbf{T} - \nabla \cdot \left(\epsilon^{\bar{\bar{\alpha}}} \mathbf{t}^{\bar{\bar{\alpha}}}\right) = 0 \quad \text{for } \alpha \in \mathcal{J}. \end{aligned} \tag{1.8}$$

The elements of $\mathcal{M}_*^{\bar{\bar{\alpha}}}$ constitute the mass conservation equation for entity α, which can be written as

$$\mathcal{M}_*^{\bar{\bar{\alpha}}} := \frac{\mathrm{D}^{\bar{\alpha}}\left(\epsilon^{\bar{\bar{\alpha}}} \rho^{\alpha}\right)}{\mathrm{D}t} + \epsilon^{\bar{\bar{\alpha}}} \rho^{\alpha} \mathbf{I} : \mathbf{d}^{\bar{\bar{\alpha}}} - \sum_{\kappa \in \mathcal{J}_{c\alpha}} {}^{\kappa \to \alpha}M = 0 \quad \text{for } \alpha \in \mathcal{J}. \tag{1.9}$$

For two-fluid-phase flow, we note that the set of entities consists of the phases, interfaces, and common curve such that the index set is

$$\mathcal{J} = \{w, n, s, wn, ws, ns, wns\} \tag{1.10}$$

As an example of the connected sets, the connected set of higher- and lower-dimensional entities for the *wn* interface is

$$\mathcal{J}_{cwn}^{+} = \{w, n\} \tag{1.11}$$

and

$$\mathcal{J}_{cwn}^{-} = \{wns\}, \tag{1.12}$$

respectively. We are considering the connected set of the solid phase to include the common curve.

1.3.3 Entropy Balance

In addition to the conservation equations, an entropy balance equation may be formulated for each entity. The microscale equation denoted as $\mathcal{S}_\alpha$ is written

$$\begin{aligned} \mathcal{S}_\alpha := & \frac{\partial^{(n)} \eta_\alpha}{\partial t} + \nabla^{(n)} \cdot (\eta_\alpha \mathbf{v}_\alpha) - b_\alpha - \sum_{\kappa \in \mathcal{J}_{c\alpha}^{+}} \frac{\eta_\kappa}{\rho_\kappa} {}^{\kappa \to \alpha}M - \nabla^{(n)} \cdot \left(\mathbf{I}_\alpha^{(n)} \cdot \varphi_\alpha\right) = \Lambda_\alpha \\ & \text{for } \alpha \in \mathcal{J}; n = 3 - \dim \alpha. \end{aligned} \tag{1.13}$$

Application of the averaging theorems Equations 1.1 and 1.3 to this equation yields the macroscale entropy balance given by

$$\mathcal{S}^{\bar{\bar{\alpha}}} := \frac{\partial \eta^{\bar{\bar{\alpha}}}}{\partial t} + \nabla \cdot \left(\eta^{\bar{\bar{\alpha}}} \mathbf{v}^{\bar{\alpha}} \right) - \epsilon^{\bar{\bar{\alpha}}} b^{\alpha} - \sum_{\kappa \in \mathcal{J}_{c\alpha}} \overset{\kappa \to \alpha}{M} \, \overline{\overline{\eta}}^{\alpha,\kappa} - \sum_{\kappa \in \mathcal{J}_{c\alpha}} \overset{\kappa \to \alpha}{\Phi} - \nabla \cdot \left(\epsilon^{\bar{\bar{\alpha}}} \varphi^{\bar{\bar{\alpha}}} \right) = \Lambda^{\bar{\bar{\alpha}}} \quad \text{for } \alpha \in \mathcal{J}. \tag{1.14}$$

As with the conservation equations, it will prove convenient to write this equation in terms of the material derivative such that we have

$$\mathcal{S}_{*}^{\bar{\bar{\alpha}}} := \frac{\mathrm{D}^{\bar{\alpha}} \eta^{\bar{\bar{\alpha}}}}{\mathrm{D}t} + \eta^{\bar{\bar{\alpha}}} \mathbf{I} : \mathbf{d}^{\bar{\alpha}} - \epsilon^{\bar{\bar{\alpha}}} b^{\alpha} - \sum_{\kappa \in \mathcal{J}_{c\alpha}} \overset{\kappa \to \alpha}{M} \, \overline{\overline{\eta}}^{\alpha,\kappa} - \sum_{\kappa \in \mathcal{J}_{c\alpha}} \overset{\kappa \to \alpha}{\Phi} - \nabla \cdot \left(\epsilon^{\bar{\bar{\alpha}}} \varphi^{\bar{\bar{\alpha}}} \right) = \Lambda^{\bar{\bar{\alpha}}} \quad \text{for } \alpha \in \mathcal{J}. \tag{1.15}$$

We observe that the quantities that appear in this balance equation do not appear in the conservation equations. To make use of this equation in conjunction with those conservation equations, two steps are taken. First, the inter-entity exchange terms will drop out if one sums the entropy balance equation over all entities. This gives us

$$\sum_{\alpha \in \mathcal{J}} \mathcal{S}_{*}^{\bar{\bar{\alpha}}} = \sum_{\alpha \in \mathcal{J}} \left[\frac{\mathrm{D}^{\bar{\alpha}} \eta^{\bar{\bar{\alpha}}}}{\mathrm{D}t} + \eta^{\bar{\bar{\alpha}}} \mathbf{I} : \mathbf{d}^{\bar{\alpha}} - \epsilon^{\bar{\bar{\alpha}}} b^{\alpha} - \nabla \cdot \left(\epsilon^{\bar{\bar{\alpha}}} \varphi^{\bar{\bar{\alpha}}} \right) \right] = \sum_{\alpha \in \mathcal{J}} \Lambda^{\bar{\bar{\alpha}}}. \tag{1.16}$$

From the second law of thermodynamics, we know that entropy generation due to irreversible processes is nonnegative. Therefore, we know that

$$\sum_{\alpha \in \mathcal{J}} \Lambda^{\bar{\bar{\alpha}}} \geq 0. \tag{1.17}$$

The second step in making the entropy inequality helpful in conjunction with the conservation equations is the postulation of a thermodynamic formalism that relates entropy to internal energy. An approach to this problem is provided in the next subsection.

1.3.4 Thermodynamic Formalism

The simplest thermodynamic formulation that can be employed is classical irreversible thermodynamics (CIT) [5,11,18]. We will use this formalism here because of its simplicity and the fact that it indeed describes the thermodynamic behavior of many important systems. The approach employed is to make use of the known thermodynamic relations at the microscale and then average them to the macroscale. By using this approach, we ensure that all thermodynamic quantities are well defined at the macroscale and that thermodynamic information is transferred consistently between scales. The thermodynamic formalism can be developed using a common notation for all entities except the solid. Here, we assume that the solid is elastic, and we provide the thermodynamic relations consistent with that specification.

Classical thermodynamics provides thermodynamic properties of equilibrium systems. Using the CIT approach, we make use of a local equilibrium assumption such that the thermodynamic relations are considered to apply at each point in the system even though the properties that are constant when the system is at equilibrium have spatial and temporal variation. It is important to note that the local equilibrium assumption is enforced at the microscale but is not imposed separately at a larger

scale when the larger-scale equations are obtained by averaging the smaller scale thermodynamic relations. The impact and importance of nonlocal equilibrium at the larger scale in the thermodynamic relations are obtained through the averaging process that requires consistency between scales.

The thermodynamics of fluid phases, interfaces, and common curves are all defined by the Euler form of the energy equation per region of the entity written as

$$E_\alpha = \theta_\alpha \eta_\alpha + \mu_\alpha \rho_\alpha - P_\alpha \quad \text{for } \alpha \in \mathcal{J}_{\backslash s}. \tag{1.18}$$

where

$P_\alpha = p_\alpha$ is pressure when α denotes a fluid phase
$P_\alpha = -\gamma_\alpha$ for an interface where γ_α is the interfacial tension
$P_\alpha = \gamma_\alpha$ for a common curve where γ_α is the curvilinear tension of the curve

The derivative of this equation may be written as

$$\mathrm{d}^{(n)} E_\alpha = \theta_\alpha \mathrm{d}^{(n)} \eta_\alpha + \mu_\alpha \mathrm{d}^{(n)} \rho_\alpha \quad \text{for } \alpha \in \mathcal{J}_{\backslash s}, \tag{1.19}$$

where

$\mathrm{d}^{(n)}$ is a differential operator
the superscript (n) constrains the differentiation to remain within the entity when α is of dimensionality $3 - n$

With $\mathrm{d}^{(n)}$ replaced by $\partial^{(n)}/\partial t$ in Equation 1.19, averaging theorem Equation 1.3 can be applied to obtain a macroscale thermodynamic equation involving the time derivative. If $\mathrm{d}^{(n)}$ is replaced by the gradient operator, $\nabla^{(n)}$ in Equation 1.19, the spatial averaging theorem, Equation 1.2, can be used to obtain an expression for the macroscale gradient of energy. Then summation of these two results after dotting the gradient expression with $\mathbf{v}^{\bar{\alpha}}$ yields the averaged form of the thermodynamic relation given by

$$\begin{aligned}
\mathcal{T}_*^{\bar{\alpha}} := & \frac{\mathrm{D}^{\bar{\alpha}} E^{\bar{\bar{\alpha}}}}{\mathrm{D}t} - \theta^{\bar{\bar{\alpha}}} \frac{\mathrm{D}^{\bar{\alpha}} \eta^{\bar{\bar{\alpha}}}}{\mathrm{D}t} - \mu^{\bar{\alpha}} \frac{\mathrm{D}^{\bar{\alpha}} \left(\epsilon^{\bar{\bar{\alpha}}} \rho^{\alpha} \right)}{\mathrm{D}t} \\
& + \sum_{\kappa \in \mathcal{J}_{c\alpha}} \left\langle \mathbf{n}_\alpha \cdot \left(\mathbf{v}_\kappa - \mathbf{v}^{\bar{s}} \right) P_\alpha \right\rangle_{\Omega_\kappa, \Omega} \\
& + \left\langle \eta_\alpha \frac{\mathrm{D}^{(n)\bar{s}} \left(\theta_\alpha - \theta^{\bar{\bar{\alpha}}} \right)}{\mathrm{D}t} \right\rangle_{\Omega_\alpha, \Omega} + \left\langle \rho_\alpha \frac{\mathrm{D}^{(n)\bar{s}} \left(\mu_\alpha - \mu^{\bar{\alpha}} \right)}{\mathrm{D}t} \right\rangle_{\Omega_\alpha, \Omega} \\
& - \left[\eta^{\bar{\bar{\alpha}}} \nabla \theta^{\bar{\bar{\alpha}}} - \nabla \cdot \left\langle \mathbf{l}_\alpha^{(n)} P_\alpha \right\rangle_{\Omega_\alpha, \Omega} + \epsilon^{\bar{\bar{\alpha}}} \rho^{\alpha} \nabla \mu^{\bar{\alpha}} \right] \cdot \left(\mathbf{v}^{\bar{\alpha}} - \mathbf{v}^{\bar{s}} \right) \\
& - \nabla \cdot \left\langle \left(\mathbf{l} - \mathbf{l}_\alpha^{(n)} \right) \cdot \left(\mathbf{v}_\alpha - \mathbf{v}^{\bar{\alpha}} \right) P_\alpha \right\rangle_{\Omega_\alpha, \Omega} - \left\langle \left(\mathbf{l} - \mathbf{l}_\alpha^{(n)} \right) P_\alpha \right\rangle_{\Omega_\alpha, \Omega} : \mathbf{d}^{\bar{\bar{\alpha}}} \\
& - \left\langle \nabla^{(n)} \cdot \mathbf{l}_\alpha^{(n)} \cdot \left(\mathbf{v}_\alpha - \mathbf{v}^{\bar{s}} \right) P_\alpha \right\rangle_{\Omega_\alpha, \Omega} \\
& + \left\langle \eta_\alpha \left(\mathbf{v}_\alpha - \mathbf{v}^{\bar{s}} \right) \cdot \left(\mathbf{l} - \mathbf{l}_\alpha^{(n)} \right) \right\rangle_{\Omega_\alpha, \Omega} \cdot \nabla \theta^{\bar{\bar{\alpha}}} \\
& + \left\langle \rho_\alpha \left(\mathbf{v}_\alpha - \mathbf{v}^{\bar{s}} \right) \cdot \left(\mathbf{l} - \mathbf{l}_\alpha^{(n)} \right) \right\rangle_{\Omega_\alpha, \Omega} \cdot \nabla \mu^{\bar{\alpha}} = 0 \quad \text{for } \alpha \in \mathcal{J}_{\backslash s}.
\end{aligned} \tag{1.20}$$

We emphasize that this expression makes use of the local equilibrium approximation at the microscale but does not require this condition to hold at the macroscale.

Although it is not a thermodynamic condition, the equation for the rate of change of the gravitational potential is handled similarly to the thermodynamic condition. Because $\Psi_\alpha = \rho_\alpha \psi_\alpha$, the derivative of this expression is

$$\mathrm{d}^{(n)}\Psi_\alpha - \psi_\alpha \mathrm{d}^{(n)}\rho_\alpha - \rho_\alpha \mathrm{d}^{(n)}\psi_\alpha = 0 \quad \text{for } \alpha \in \mathcal{J}. \tag{1.21}$$

The differential $\mathrm{d}^{(n)}$ may be replaced, successively, by the partial time derivative and gradient operators with the averaging theorems applied to the resulting equations. Then, if the resulting equation in terms of the gradient is dotted with $\mathbf{v}^{\bar{\alpha}}$ and added to the partial time derivative equation, the result is

$$\mathcal{T}_{\mathcal{G}_*}^{\bar{\bar{\alpha}}} := \frac{\mathrm{D}^{\bar{\alpha}}\Psi^{\bar{\bar{\alpha}}}}{\mathrm{D}t} - \psi^{\bar{\alpha}} \frac{\mathrm{D}^{\bar{\alpha}}\left(\epsilon^{\bar{\bar{\alpha}}}\rho^{\alpha}\right)}{\mathrm{D}t} - \left\langle \rho_\alpha \frac{\mathrm{D}^{(n)\bar{s}}\psi^{\bar{\alpha}}}{\mathrm{D}t} \right\rangle_{\Omega_\alpha,\Omega} - \epsilon^{\bar{\bar{\alpha}}}\rho^{\alpha}\nabla\psi^{\bar{\alpha}} \cdot \left(\mathbf{v}^{\bar{\alpha}} - \mathbf{v}^{\bar{s}}\right)$$
$$+ \left\langle \rho_\alpha \left(\mathbf{v}_\alpha - \mathbf{v}^{\bar{s}}\right) \cdot \left(\mathbf{I} - \mathbf{I}_\alpha^{(n)}\right) \right\rangle_{\Omega_\alpha,\Omega} \cdot \nabla\psi^{\bar{\alpha}} = 0 \quad \text{for } \alpha \in \mathcal{J}. \tag{1.22}$$

This equation added to Equation 1.20 provides a relation for the rate of change of macroscale internal plus potential energy for fluid phases, interfaces, and the common curve.

A potentially fertile area for additional research is the representation of solid phases at the macroscale. Here, we adopt a relatively simple model of the solid as an elastic material, which can be formulated as

$$E_s = \theta_s \eta_s + \sigma_s : \frac{\mathbf{C}_s}{j_s} + \mu_s \rho_s, \tag{1.23}$$

where

σ_s is a stress tensor
$\mathbf{C}_s$ is Green's deformation tensor
j_s is the Jacobian

The derivative of this equation may be written

$$\mathrm{d}E_s = \theta_s \, \mathrm{d}\eta_s + \sigma_s : \mathrm{d}\left(\frac{\mathbf{C}_s}{j_s}\right) + \mu_s \, \mathrm{d}\rho_s. \tag{1.24}$$

If the arbitrary differential in Equation 1.24 is replaced successively by the partial time derivative and gradient operators, the resulting equations can be averaged making use of the time and space averaging theorems. With the gradient expression dotted with $\mathbf{v}^{\bar{s}}$ added to the time derivative

expression, the resulting expression for the relation among the rates of change of macroscale thermodynamic properties of the solid is

$$\mathcal{T}_*^{\bar{\bar{s}}} := \frac{\mathrm{D}^{\bar{s}} E^{\bar{\bar{s}}}}{\mathrm{D}t} - \theta^{\bar{\bar{s}}} \frac{\mathrm{D}^{\bar{s}} \eta^{\bar{\bar{s}}}}{\mathrm{D}t} - \mu^{\bar{s}} \frac{\mathrm{D}^{\bar{s}} \left(\epsilon^{\bar{\bar{s}}} \rho^{s} \right)}{\mathrm{D}t} - \sum_{\kappa \in \mathcal{J}_{\mathrm{cs}}} \left\langle \mathbf{n}_s \cdot \left(\mathbf{v}_\kappa - \mathbf{v}_s \right) \sigma_s : \frac{\mathbf{C}_s}{j_s} \right\rangle_{\Omega_\kappa, \Omega}$$

$$- \sum_{\kappa \in \mathcal{J}_{\mathrm{cs}}} \left\langle \mathbf{n}_s \cdot \mathbf{t}_s \cdot \left(\mathbf{v}_s - \mathbf{v}^{\bar{s}} \right) \right\rangle_{\Omega_\kappa, \Omega} + \left\langle \eta_s \frac{\mathrm{D}^{\bar{s}} \left(\theta_s - \theta^{\bar{\bar{s}}} \right)}{\mathrm{D}t} \right\rangle_{\Omega_s, \Omega}$$

$$+ \left\langle \rho_s \frac{\mathrm{D}^{\bar{s}} \left(\mu_s - \mu^{\bar{s}} \right)}{\mathrm{D}t} \right\rangle_{\Omega_s, \Omega} - \nabla \cdot \left\langle \left(\mathbf{t}_s - \sigma_s : \frac{\mathbf{C}_s}{j_s} \mathbf{I} \right) \cdot \left(\mathbf{v}_s - \mathbf{v}^{\bar{s}} \right) \right\rangle_{\Omega_s, \Omega}$$

$$- \epsilon^{\bar{\bar{s}}} \mathbf{t}^{s} : \mathbf{d}^{\bar{s}} + \epsilon^{\bar{\bar{s}}} \sigma^{\bar{s}} : \frac{\mathbf{C}^{s}}{j^{s}} \mathbf{I} : \mathbf{d}^{\bar{s}} + \left\langle \left(\nabla \cdot \mathbf{t}_s - \nabla \sigma_s : \frac{\mathbf{C}_s}{j_s} \right) \cdot \left(\mathbf{v}_s - \mathbf{v}^{\bar{\bar{s}}} \right) \right\rangle_{\Omega_s, \Omega} = 0. \tag{1.25}$$

This expression makes use of the microscale local equilibrium approximation and also accounts for the fact that a concentrated force can act on the solid surface at common curves and common points. The equation for the rate of change of gravitational potential for the solid phase is obtained from Equation 1.22.

1.3.5 Evolution Equations

Unique to the TCAT approach in comparison to other averaging methods is the incorporation of the kinematics of the space occupied by a phase, and of the shape and extent of an interface between phases and of the common curve on the solid surface into the full formulation [26,28,31]. Kinematics of irregular geometries are difficult to describe exactly, so we rely on approximations that are based on the averaging theorems, in particular Equations 1.2 and 1.3 with $f_\alpha = 1$. The gradient theorem becomes

$$0 = \nabla \epsilon^{\bar{\bar{\alpha}}} - \nabla \cdot \left\langle \mathbf{l} - \mathbf{l}_\alpha^{(n)} \right\rangle_{\Omega_\alpha, \Omega} - \left\langle \nabla^{(n)} \cdot \mathbf{l}_\alpha^{(n)} \right\rangle_{\Omega_\alpha, \Omega} + \sum_{\kappa \in \mathcal{J}_{\mathrm{c}\alpha}} \left\langle \mathbf{n}_\alpha \right\rangle_{\Omega_\kappa, \Omega}, \tag{1.26}$$

while the time derivative theorem simplifies to

$$0 = \frac{\partial \epsilon^{\bar{\bar{\alpha}}}}{\partial t} + \nabla \cdot \left\langle \left(\mathbf{l} - \mathbf{l}_\alpha^{(n)} \right) \cdot \mathbf{v}_\alpha \right\rangle_{\Omega_\alpha, \Omega} + \left\langle \nabla^{(n)} \cdot \mathbf{l}_\alpha^{(n)} \cdot \mathbf{v}_\alpha \right\rangle_{\Omega_\alpha, \Omega} - \sum_{\kappa \in \mathcal{J}_{\mathrm{c}\alpha}} \left\langle \mathbf{n}_\alpha \cdot \mathbf{v}_\kappa \right\rangle_{\Omega_\kappa, \Omega}. \tag{1.27}$$

These two equations provide relations among the geometric density of the entity of interest, an orientation tensor, and averages of the velocities of the entities.

It is important to recognize that the velocity of an entity is not necessarily equal to the velocity of the material in the entity except, for the case of an interfacial area or a common curve, in the directions normal to the entity. As might be expected, the velocities of the entities in their tangential directions do not appear in the preceding two equations. The challenge that arises is relating the changes of extent of one entity to that of another entity. For example, if a phase is

spherical, it is easy to relate the rate of change in the size of the sphere to the rate of change of the surface area of the sphere; for the case of complicated phase geometries, phase boundaries, and curve lengths, such a relation cannot be obtained. Nevertheless, Equations 1.26 and 1.27 provide exact relations that can be approximated to obtain appropriate macroscale relations. These results can then be studied because the larger-scale variables will be specified in terms of microscale variables.

To obtain an evolution form in terms of a material derivative moving with the macroscale solid phase velocity, we take the dot product of Equation 1.26 with $\mathbf{v}^{\bar{s}}$ and add this to Equation 1.27. After minor rearrangement, this gives

$$\frac{\mathrm{D}^{\bar{s}}\epsilon^{\bar{\bar{\alpha}}}}{\mathrm{D}t}+\nabla\cdot\left\langle\left(\mathbf{l}-\mathbf{l}_{\alpha}^{(n)}\right)\cdot\left(\mathbf{v}_{\alpha}-\mathbf{v}^{\bar{s}}\right)\right\rangle_{\Omega_{\alpha},\Omega}+\left\langle\mathbf{l}-\mathbf{l}_{\alpha}^{(n)}\right\rangle_{\Omega_{\alpha},\Omega}:\mathbf{d}^{\bar{s}}$$
$$+\left\langle\nabla^{(n)}\cdot\mathbf{l}_{\alpha}^{(n)}\cdot\left(\mathbf{v}_{\alpha}-\mathbf{v}^{\bar{s}}\right)\right\rangle_{\Omega_{\alpha},\Omega}-\sum_{\kappa\in\mathcal{J}_{\bar{c}\alpha}}\left\langle\mathbf{n}_{\alpha}\cdot\left(\mathbf{v}_{\kappa}-\mathbf{v}^{\bar{s}}\right)\right\rangle_{\Omega_{\kappa},\Omega}=0\quad\text{for}\,\alpha\in\mathcal{J}. \tag{1.28}$$

Although this equation describes the evolution of the various geometric entities, it is of limited use as is because not all of the quantities expressed with the averaging operator can be evaluated in terms of the set of macroscale variables that arise in averaging conservation equations. The complex geometries and distributions of the entities also mean that robust approximate evaluations are difficult to identify. Nevertheless, these equations are important constraints on the behavior of the system. The last term on the left side of Equation 1.28 expresses the fact that the change in distribution of an entity is related to changes in the distribution of lower-dimensional entities. For the two-fluid-phase system of concern here, we make some approximations that can be revisited if significant errors in subsequent macroscale simulations or insights gained from microscale simulations suggest a need to do so.

The derivation of an approximate form of Equation 1.28 is a rather involved process and can be found in [28]. Here, we provide the equation that results when the solid deformation is much slower than fluid redistribution, and we are interested in the rate of change of the *wn* interface. Elements of the physical processes that can cause $\epsilon^{\bar{\bar{wn}}}$ to evolve are the normal velocity of the interface, interfacial curvature changes, and the movement of the common curve on the solid surface. The governing approximate equation is [26,28]

$$\frac{\mathrm{D}^{\bar{s}}\epsilon^{\bar{\bar{wn}}}}{\mathrm{D}t}+\nabla\cdot\left[\epsilon^{\bar{\bar{wn}}}\left(\mathbf{w}^{wn}-\mathbf{G}^{wn}\cdot\mathbf{v}^{\bar{s}}\right)\right]-J_{w}^{wn}\frac{\mathrm{D}^{\bar{s}}\epsilon^{\bar{\bar{w}}}}{\mathrm{D}t}-\hat{k}^{wn}\left(\epsilon_{\mathrm{eq}}^{\bar{\bar{wn}}}-\epsilon^{\bar{\bar{wn}}}\right)-\cos\varphi^{\bar{\bar{ws}},\bar{\bar{wn}}}\left(\epsilon^{\bar{\bar{ws}}}+\epsilon^{\bar{\bar{ns}}}\right)\frac{\mathrm{D}^{\bar{s}}\chi_{s}^{\bar{\bar{ws}}}}{\mathrm{D}t}=0. \tag{1.29}$$

The terms in this equation are, in order, the rate of change of *wn* interface density, the net outward flux of $\epsilon^{\bar{\bar{wn}}}$, increase in $\epsilon^{\bar{\bar{wn}}}$ caused by a change in the volume fraction of fluid phase *w*, relaxation of $\epsilon^{\bar{\bar{wn}}}$ to an equilibrium configuration, and the change in $\epsilon^{\bar{\bar{wn}}}$ due to movement of the common curve that is the boundary of the interface. The quantity $\mathbf{G}^{wn}$ is an orientation tensor that accounts for the fact that the *wn* interface may have a preferred orientation direction.

For the common curve, more approximations are needed. These approximations are not as robust as those for the interface, but the errors are not as important if the common curve dynamics have less importance in modeling the overall system behavior. The equation that results is [26,28]

$$\frac{\mathrm{D}^{\bar{s}}\epsilon^{\bar{\bar{wns}}}}{\mathrm{D}t}+\nabla\cdot\left[\epsilon^{\bar{\bar{wns}}}\left(\mathbf{w}^{wns}-\mathbf{G}^{wns}\cdot\mathbf{v}^{\bar{s}}\right)\right]+\kappa_{\mathrm{G}}^{wns}\left(\epsilon^{\bar{\bar{ws}}}+\epsilon^{\bar{\bar{ns}}}\right)\frac{\mathrm{D}^{\bar{s}}\chi_{s}^{\bar{\bar{ws}}}}{\mathrm{D}t}-\hat{k}^{wns}\left(\epsilon_{\mathrm{eq}}^{\bar{\bar{wns}}}-\epsilon^{\bar{\bar{wns}}}\right)=0. \tag{1.30}$$

This equation relates the rate of change of common curve length per volume, respectively, to the net outward flux of the common curve, the movement of the curve along a solid surface that leads to its expansion or contraction, and the relaxation of the common curve length to its equilibrium length due to stretching. This latter term is expected to be negligible for the case of a two-fluid system when the solid does not deform.

1.3.6 Entropy Inequality

The entropy inequality is constrained by the conservation equations, the body force potential equation, and the thermodynamic relations such that the material derivatives are eliminated as far as possible. This strategy serves to express the rate of entropy generation as a product of independent forces and fluxes, each of which is zero at equilibrium. The constrained form is expressed as

$$\sum_{\alpha\in\mathcal{J}}\left[\mathcal{S}_*^{\bar{\bar{\alpha}}}-\frac{1}{\theta^{\bar{\bar{\alpha}}}}\mathcal{E}_*^{\bar{\bar{\alpha}}}+\frac{1}{\theta^{\bar{\bar{\alpha}}}}\mathbf{v}^{\bar{\alpha}}\cdot\boldsymbol{\mathcal{P}}_*^{\bar{\bar{\alpha}}}+\frac{1}{\theta^{\bar{\bar{\alpha}}}}\left(\mu^{\bar{\alpha}}+\psi^{\bar{\alpha}}-\frac{\mathbf{v}^{\bar{\alpha}}\cdot\mathbf{v}^{\bar{\alpha}}}{2}+K_E^{\bar{\bar{\alpha}}}\right)\mathcal{M}_*^{\bar{\bar{\alpha}}}+\frac{1}{\theta^{\bar{\bar{\alpha}}}}\mathcal{T}_*^{\bar{\bar{\alpha}}}+\frac{1}{\theta^{\bar{\bar{\alpha}}}}\mathcal{T}_{\mathcal{G}^*}^{\bar{\bar{\alpha}}}\right]=\sum_{\alpha\in\mathcal{J}}\Lambda^{\bar{\bar{\alpha}}}\geq 0. \tag{1.31}$$

After substitution of the appropriate conservation and thermodynamic equations into this equation, terms can be collected and canceled. For this study, we also employ approximations consistent with an isothermal system, a rigid solid, no mass exchange between entities, and massless interfaces and common curve to obtain

$$\begin{aligned}
&\sum_{\alpha\in\mathcal{J}_\mathrm{f}}\frac{1}{\theta}\left(\epsilon^{\bar{\bar{\alpha}}}\mathbf{t}^{\bar{\bar{\alpha}}}+\epsilon^{\bar{\bar{\alpha}}}p^{\alpha}\mathbf{I}\right):\mathbf{d}^{\bar{\bar{\alpha}}}+\sum_{\alpha\in\mathcal{J}_\mathrm{I}}\frac{1}{\theta}\left[\epsilon^{\bar{\bar{\alpha}}}\mathbf{t}^{\bar{\bar{\alpha}}}-\epsilon^{\bar{\bar{\alpha}}}\gamma^{\alpha}\left(\mathbf{I}-\mathbf{G}^{\alpha}\right)\right]:\mathbf{d}^{\bar{\bar{\alpha}}}+\frac{1}{\theta}\left[\epsilon^{\overline{\overline{wns}}}\mathbf{t}^{\overline{\overline{wns}}}+\epsilon^{\overline{\overline{wns}}}\gamma^{wns}\left(\mathbf{I}-\mathbf{G}^{wns}\right)\right]:\mathbf{d}^{\overline{\overline{wns}}}\\
&+\left\{\sum_{\alpha\epsilon\mathcal{J}_\mathrm{f}}\frac{1}{\theta}\left\{\nabla\left(\epsilon^{\bar{\bar{\alpha}}}p^{\alpha}\right)-\epsilon^{\bar{\bar{\alpha}}}\rho^{\alpha}\nabla\left(\mu^{\bar{\alpha}}+K_E^{\bar{\bar{\alpha}}}+\psi^{\bar{\alpha}}\right)-\epsilon^{\bar{\bar{\alpha}}}\rho^{\alpha}\mathbf{g}^{\bar{\alpha}}+\sum_{\kappa\in\mathcal{J}_{c\alpha}}^{\alpha\to\kappa}\mathbf{T}\right\}\cdot\left(\mathbf{v}^{\bar{\alpha}}-\mathbf{v}^{\bar{\bar{s}}}\right)\right.\\
&-\sum_{\alpha\in\mathcal{J}_\mathrm{I}}\frac{1}{\theta}\left\{\nabla\cdot\left[\left(\mathbf{I}-\mathbf{G}^{\alpha}\right)\epsilon^{\bar{\bar{\alpha}}}\gamma^{\alpha}\right]+\sum_{\kappa\in\mathcal{J}_{c\alpha}^{+}}^{\kappa\to\alpha}\mathbf{T}-\sum^{\alpha\to wns}\mathbf{T}\right\}\cdot\left(\mathbf{v}^{\bar{\alpha}}-\mathbf{v}^{\bar{\bar{s}}}\right)\\
&+\frac{1}{\theta}\left\{\nabla\cdot\left[\left(\mathbf{I}-\mathbf{G}^{wns}\right)\epsilon^{\overline{\overline{wns}}}\gamma^{wns}\right]-\sum_{\kappa\in\mathcal{J}_{\mathrm{cwns}}^{+}}^{\kappa\to wns}\mathbf{T}\right\}\cdot\left(\mathbf{v}^{\overline{wns}}-\mathbf{v}^{\bar{\bar{s}}}\right)\\
&+\frac{1}{\theta}\left[\frac{\mathrm{D}^{\bar{s}}\epsilon^{\bar{\bar{w}}}}{\mathrm{D}t}-\frac{\gamma^{wn}\hat{k}_1^{wn}\left(\epsilon^{\overline{\overline{wn}}}-\epsilon_{\mathrm{eq}}^{\overline{\overline{wn}}}\right)}{\left(p_w^{wn}-p_n^{wn}\right)}\right]\left(p_w^{wn}-p_n^{wn}-\gamma^{wn}J_w^{wn}\right)\\
&-\frac{1}{\theta}\left(\epsilon^{\overline{\overline{ws}}}+\epsilon^{\overline{\overline{ns}}}\right)\frac{\mathrm{D}^{\bar{s}}\chi_s^{\overline{\overline{ws}}}}{\mathrm{D}t}\left[\gamma_{wn}^{wns}\cos\varphi^{\overline{\overline{ws,wn}}}+\gamma_{ws}^{wns}-\gamma_{ns}^{wns}+\gamma^{wns}\kappa_G^{\overline{\overline{wns}}}\right]\\
&=\sum_{\alpha\in\mathcal{J}}\Lambda^{\bar{\bar{\alpha}}}\geq 0.
\end{aligned} \tag{1.32}$$

The manipulations involved in obtaining this equation are extensive, but not particularly difficult. Detailed examples of the steps involved in the algebra may be found in [28]. Equation 1.32 provides the independent force–flux pairings that are used to obtain linear relations among forces and fluxes. The entropy inequality is listed here because it is a precursor for any two-fluid-phase flow model that could be formulated with the restrictions specified preceding this equation. Because each member of the set of forces and each member of the set of fluxes is independent of all other members in their respective set, each force and flux must be zero at equilibrium. The simplest condition that this suggests is a linear relation between each flux and the forces. Here, for simplicity and with some limited generality, we will make use of these linearizations with each flux considered to be linear in only its conjugate force rather than all forces. Thus, for example, we can deduce from the third line from the bottom of Equation 1.32 that

$$\frac{\mathrm{D}^{\bar{s}}\epsilon^{\bar{\bar{w}}}}{\mathrm{D}t} - \frac{\gamma^{wn}\hat{k}_1^{wn}\left(\epsilon^{\bar{\bar{wn}}} - \epsilon_{\mathrm{eq}}^{\bar{\bar{wn}}}\right)}{\left(p_w^{wn} - p_n^{wn}\right)} = \hat{c}\left(p_w^{wn} - p_n^{wn} - \gamma^{wn}J_w^{wn}\right) \tag{1.33}$$

is an expression that describes the relaxation of the capillary pressure at the interface due to the difference in pressures between the phases at the interface. Furthermore, $\hat{c}$ must be nonnegative to ensure that the entropy inequality is not violated. If linearized approximations of fluxes in terms of conjugate forces are found to be inadequate to describe the system, more complex forms can be postulated that must still be consistent with Equation 1.32.

1.4 MODEL FORMULATION

The linearization of the force–flux pairs and substitution into the conservation equations leads to a closed set of conservation and balance equations under simple conditions of constant-density fluids, an immobile solid, an isothermal system, no mass exchange between phases, and massless interfaces and common curve. Additionally, the flow in the porous medium is considered to be slow such that the inertial terms in the momentum equation can be neglected. Mass conservation for the fluid phases is accounted for with

$$\frac{\mathrm{D}^{\bar{\alpha}}s^{\bar{\bar{\alpha}}}}{\mathrm{D}t} + s^{\bar{\bar{\alpha}}}\mathbf{I} : \mathbf{d}^{\bar{\bar{\alpha}}} = 0 \quad \text{for } \alpha \in \mathcal{J}_{\mathrm{f}}, \tag{1.34}$$

and

$$s^{\bar{\bar{n}}} = 1 - s^{\bar{\bar{w}}}. \tag{1.35}$$

The flow equations for the phases are obtained as in [25] with

$$\nabla p^{\alpha} - \rho^{\alpha}\mathbf{g} + \hat{R}_w^{\alpha}\mathbf{v}^{\bar{w}} + \hat{R}_n^{\alpha}\mathbf{v}^{\bar{n}} + \hat{R}^{p\alpha}\epsilon\nabla s^{\bar{\bar{\alpha}}} = \mathbf{0} \quad \text{for } \alpha \in \mathcal{J}_{\mathrm{f}}, \tag{1.36}$$

where the last term on the left side of the equation accounts for the impact of the gradient in the saturation on the volumetric average of a microscopic pressure field. When this term is negligible, the flow equations are similar to Darcy's law with cross coupling of the flow velocities included.

Equations 1.34 through 1.36 consist of nine scalar equation components in the 10 unknowns comprising $\mathcal{V}$ where

$$\mathcal{V} = \left\{s^{\bar{\bar{w}}}, s^{\bar{\bar{n}}}, \mathbf{v}^{\bar{w}}, \mathbf{v}^{\bar{n}}, p^{w}, p^{n}\right\}. \tag{1.37}$$

The usual procedure for making up for the deficit of equations is to require the difference in phase pressures to be equal to some function of saturation, $f(s^{\bar{\bar{w}}})$, such that

$$p^n - p^w = f(s^{\bar{\bar{w}}}). \tag{1.38}$$

This relation is demonstrably inadequate in a number of ways. No function $f(s^{\bar{\bar{w}}})$ has been found that is single valued. The function employed is based on data claimed to be collected at equilibrium, while the function itself is applied in dynamic situations. Efforts to equate $f(s^{\bar{\bar{w}}})$ to the capillary pressure merely demonstrate that, while the function is somewhat related to capillary pressure, other factors enter into the formalism due to the fact that the well-defined microscale capillary pressure is replaced by some approximate macroscale analog.

The TCAT approach suggests a more comprehensive method for closing the equation system. This method includes the fluid–fluid interfacial area per volume, $\epsilon^{\bar{\bar{wn}}}$, as an unknown. It also requires that the macroscale capillary pressure, denoted p^{wn}, and an equilibrium value for $\epsilon^{\bar{\bar{wn}}}$ be specified as functions of the problem variables. In the TCAT formulation, p^{wn} arises in the analysis as the intrinsic average over the *wn* interface of $\gamma_{wn}J_w$, the interfacial tension multiplied by the interfacial curvature, $J_w = \nabla' \cdot \mathbf{n}_w$. For the case where γ_{wn} is constant, this average is equal to the product of the macroscale averages γ^{wn} and J_w^{wn}. Inclusion of these variables raises the equation deficit to four, which is addressed as follows based on guidance from the entropy inequality discussed earlier and the evolution equations.

The difference in pressures of the fluid phases is modeled as

$$p^n - p^w = p^{wn} - \frac{\epsilon}{\hat{c}^{wn}} \frac{\partial s^{\bar{\bar{w}}}}{\partial t} + \frac{\gamma^{wn} \hat{k}_1^{wn} \left(\epsilon^{\bar{\bar{wn}}} - \epsilon_{\text{eq}}^{\bar{\bar{wn}}} \right)}{\hat{c}^{wn} \left(p^w - p^n \right)}, \tag{1.39}$$

where

$$p^{wn} = p^{wn} \left(s^{\bar{\bar{w}}}, \epsilon^{\bar{\bar{wn}}} \right) \tag{1.40}$$

and

$$\epsilon_{\text{eq}}^{\bar{\bar{wn}}} = \epsilon_{\text{eq}}^{\bar{\bar{wn}}} \left(p^n - p^w, s^{\bar{\bar{w}}} \right). \tag{1.41}$$

Note that in this equation set, p^{wn} depends on both saturation and the interfacial area density, and it will equal the pressure difference between the fluid phases at equilibrium. The inclusion of dependence of p^{wn} on $\epsilon^{\bar{\bar{wn}}}$ provides a better opportunity to model macroscale capillarity by approximating average interfacial curvature as a function of the volume occupied by the fluid phases and the interfacial area extent. The second and third terms on the right side of Equation 1.39 account for adjustment of the fluids during a dynamic process due, respectively, to changes in saturation and changes in interfacial area configuration.

The use of this equation set still leaves a deficit of one equation. One way that this has been handled in the past is to drop all dependences on $\epsilon^{\bar{\bar{wn}}}$ in Equations 1.39 and 1.40 such that Equation 1.41 is not needed. This approach essentially considers the relaxation to equilibrium in a system to be due solely to changes in saturation. It is typically applied in practice by adding

a term related to the rate of change of saturation to Equation 1.38 without ever considering that the interfacial area density is important. Efforts to validate this approach have not been successful (e.g., [58]).

A second approach to closure of the equation system is to include an additional equation. Such an equation is an evolution equation for the fluid–fluid interfacial area. This is obtained, most easily, as a simplified form of Equation 1.29 where the term involving the fractional wetting is neglected so that for an immobile solid

$$\frac{\partial \epsilon^{\overline{\overline{wn}}}}{\partial t} + \nabla \cdot \left(\epsilon^{\overline{\overline{wn}}} \mathbf{w}^{wn} \right) + \frac{p^{wn} \epsilon}{\gamma^{wn}} \frac{\partial s^{\overline{w}}}{\partial t} - \hat{k}^{wn} \left(\epsilon_{\text{eq}}^{\overline{\overline{wn}}} - \epsilon^{\overline{\overline{wn}}} \right) = 0, \tag{1.42}$$

where $\mathbf{w}^{wn}$ must be expressed as some function of the two-fluid-phase velocities. Additionally, we obtain the relation between $\hat{k}^{wn}$ and $\hat{k}_1^{wn}$ as

$$\hat{k}^{wn} = \left(\frac{p^{wn}}{p^n - p^w} - 1 \right) \hat{k}_1^{wn}. \tag{1.43}$$

Equations 1.34 through 1.36 supplemented by Equations 1.39 through 1.42 capture the physics of multiphase flow in porous media and account for important mechanisms that impact the system behavior not modeled in traditional models. The obvious drawback of this extended model is the additional parameters that must be determined. The values of these parameters have their roots in microscale system behavior. Therefore, if microscale equations can be solved, then the average of the solutions can be used to populate the forms of needed functions. Here, we will make use of the LBM to simulate multiphase flow and then use the results of those simulations to demonstrate some important aspects of this extended model. This demonstration suggests avenues for further research involving more general models that can be proposed based on TCAT analysis.

1.5 MICROSCALE CONSIDERATIONS

Closure of the macroscale TCAT model formulated in Equations 1.34 through 1.36 and Equations 1.39 through 1.42 requires the conversion of the general functional forms of the closure relations given by Equations 1.40 and 1.41 to specific functional forms. In addition, the closure relations given by Equations 1.42 and 1.43 contain approximations and coefficients that require evaluation. In general terms, relationships are needed among fluid pressures, fluid saturations, interfacial areas, interfacial curvatures at equilibrium, and the rate of approach to the equilibrium state. This could be dismissed as an onerous task, or it could be viewed as a necessary step if one is truly interested in obtaining a class of high-fidelity, physics-based models for two-phase flow.

Traditional two-phase-flow models require the definition of hysteretic pressure–saturation–relative permeability models and the parameters in these models, which are burdensome to determine [48]. Quite often the form of the model is assumed and the parameters estimated using surrogate means, which reduces the apparent burden. However, the difficulty with the approach in traditional models is that important aspects of the physics are being treated implicitly in the closure relation formulation, and surrogate estimates of parameters can introduce a source of error.

To advance TCAT models for two-fluid-phase flow, new methods must be developed to determine the aspects of the system that must be observed. These aspects include various types of fluid pressures depending upon the averaging region, fluid saturations, interfacial areas, curvatures of the interface, common curve lengths and curvatures, orientation tensors for interfaces and common curves, dynamic relaxation coefficients, and contact angles. The formation and characteristics of

the residual nonwetting phase are also potentially important. These detailed measures of the state of a two-fluid-phase system are of interest not only for the closure and validation of TCAT models but also because they can lead to improved fundamental understanding of the system and be used to evaluate and parameterize alternative macroscale models.

Standard macroscale experimental approaches are unable to observe many of the aspects of a two-fluid-phase porous medium system that are of interest and noted earlier, because these properties depend upon knowledge of the pore morphology and topology of the system that is not accessible by merely interpreting the total volume of each phase within the system. Likewise, destructive methods of observing the state of a two-fluid-phase system are not of much use either as they are much too inefficient to provide the level and quantity of information that it required. Thus, the information required must be obtained either through nondestructive, high-resolution experimental methods or high-resolution microscale simulation approaches.

Nondestructive, high-resolution experimental methods of observing multiphase porous medium systems have advanced greatly in recent years. In principle, many of the measures needed to close the TCAT model formulated earlier can examine and have been examined using experimental means. Two general experimental approaches are especially relevant: micromodel methods based upon image analysis [13] and high-flux photon attenuation methods [2,10,14,62,70]. Micromodel methods create a porous medium system that is thin in one dimension. Fluid displacements are then systematically studied and the state is observed using photographic and image-processing methods. While efficient and providing a means to observe all of the properties of interest, these systems are limited to those systems that are created, which are essentially 2D in nature. Because the porous medium systems of common interest are 3D in nature, and 3D systems behave much differently than 2D systems, micromodel approaches are limited in general applicability.

Alternatively, natural porous medium system can be observed using high-flux photon attenuation methods, which can be produced, for example, from a synchrotron source. This approach has the advantage of being able to study some of the details needed for TCAT model closure in real 3D systems. The disadvantages are that the facilities needed are specialized, dynamics are difficult to evaluate because of the time needed to image a system, and it is often not within reach to observe both the spatial scale of the system and the density of states needed to characterize sufficiently the equilibrium relationships sought. Therefore, while high-resolution experiments are important for advancing fundamental understanding of multiphase systems, they suffer from some drawbacks that preclude their general use for the full range of information sought.

The phase distribution morphology and topology measures needed to close the TCAT model formulated earlier can also be investigated using microscale modeling approaches. Approaches based upon idealized pore structures are embodied in pore network models, whereas discrete representation of the real porous medium systems can also be used. The key aspect of an ideal approach to microscale modeling is the ability to represent real systems of sufficient size at high resolution in a dynamic manner. Such an approach provides the means to provide all of the information needed to produce the necessary closure relations without the drawbacks associated with alternative experimental or modeling approaches. Despite the promise of microscale modeling approaches for determining closure relations, no modeling approach has yet been advanced to adequately resolve a sufficiently large porous medium system at the necessary resolution to provide a basis for determining the closure relations sought. In addition, the simulations that have been reported in the literature have not included all of the measures that arise in the TCAT model formulation detailed earlier. Thus, while microscale modeling methods hold great promise, this promise has yet to yield a sufficient foundation for formulating the closure relations that are sought.

In the following sections, we detail LBM simulation and computational geometry approaches for producing dynamic, high-resolution representations of the morphology and topology of a two-fluid-phase porous medium system. The results of these approaches can be used to motivate and guide the formulation of TCAT closure relations.

1.6 LATTICE BOLTZMANN MODELING

1.6.1 Formulation

LBMs are a class of numerical methods used to simulate fluid flow by discretely approximating the Boltzmann equation. While many LBMs exist, a desirable method has several characteristics: (1) the method should conserve mass and momentum; (2) the method should be Galilean invariant; (3) the moments modeled should be allowed to relax at different rates; (4) the approach chosen should be able to represent well-known behavior in model systems with a minimum of computational artifacts that can limit the usefulness of the results; (5) the method should be implemented using data structures, algorithms, and computational approaches that result in an efficient, scalable simulator on modern high-performance computing architectures; and (6) the simulator and computational environment must support simulations that are adequately resolved and of sufficient size to yield a representative averaging region.

An LBM simulator that possesses these characteristics was developed for multiphase porous medium systems based upon the three components common to LBMs: (1) a discrete lattice and associated sets of velocity vectors and distribution functions, (2) a collision operator expressed in terms of a set of equilibrium distribution functions that formulates the relaxation toward an equilibrium state, and (3) an evolution equation that specifies the manner in which the model state is advanced from one discrete time level to the next. We detail each of these components for the selected method in the following text.

A regular lattice space $\delta_s \mathbb{Z}_d$ is used to represent discretely phase space in d spatial dimensions. A symmetric set of discrete velocity vectors $\mathcal{E}_d = \{\mathbf{e}_i \mid i = 0,1,\ldots N\}$ characterizes the connection of each lattice site $\mathbf{x}_k \in \delta_s \mathbb{Z}_d$ to a set of neighboring lattice sites $\mathcal{X}_k = \{\mathbf{x}_{ki} \mid i = 0,1,\ldots N\}$. Additionally, a set of velocity distribution functions $\mathcal{F}_{dk} = \{f_i \mid i = 0,1,\ldots N\}$ is associated with the set $\mathcal{E}_d$ at each lattice location k. The discrete distributions and velocity vectors may be obtained from their continuous counterparts in kinetic theory based on a quadrature scheme [35]. These aspects of an LBM are often listed in shorthand form by specifying the lattice as being of a DdQq form, where $q = N + 1$ to account for standard indexing convention that starts with 0. We used a D3Q19 lattice, which specifies the discrete velocity set as

$$\mathbf{e}_i = \begin{Bmatrix} 0 & 1 & -1 & 0 & 0 & 0 & 0 & 1 & -1 & 1 & -1 & 1 & -1 & 1 & -1 & 0 & 0 & 0 & 0 \\ 0 & 0 & 0 & 1 & -1 & 0 & 0 & 1 & -1 & -1 & 1 & 0 & 0 & 0 & 0 & 1 & -1 & 1 & -1 \\ 0 & 0 & 0 & 0 & 0 & 1 & -1 & 0 & 0 & 0 & 0 & 1 & -1 & -1 & 1 & 1 & -1 & -1 & 1 \end{Bmatrix}, \tag{1.44}$$

where each column represents the components of the corresponding vector.

The 19 distributions evolve according to a multirelaxation time (MRT) form of the lattice Boltzmann equation

$$f_i(\mathbf{x}_k + \mathbf{e}_i \delta t, t_n + \delta t) - f_i(\mathbf{x}_k, t_n) = \mathcal{C}_i, \tag{1.45}$$

where δt is the time step.

The right side of Equation 1.45 is a collision term that accounts for the effects of intermolecular collisions. In practice, the form of this term is chosen to recover a desired continuum form for the microscale momentum transport equation by means of a multiscale expansion. The multirelaxation form of the collision operator is expressed in terms of moments of the distributions that are computed from the distributions using a linear transformation

$$\mathbf{m} = \mathbf{M} \cdot \mathbf{f}. \tag{1.46}$$

The vector containing the 19 distributions is **f**, and **M** is a transformation matrix. Among the moments computed are the density, which relates to the fluid pressure

$$\rho = \sum_{i=0}^{N} f_i = \frac{p}{c_s^2} = 3p, \tag{1.47}$$

and the momentum

$$\mathbf{j} = \rho \mathbf{u} = \sum_{i=0}^{N} f_i \mathbf{e}_i, \tag{1.48}$$

where c_s is the speed of sound. The velocity is

$$\mathbf{u} = \frac{\mathbf{j}}{\rho}. \tag{1.49}$$

Specific details for the construction of the remaining moments including the transformation matrix **M** and its inverse are available in the literature [19]. The MRT form allows each moment to relax toward its equilibrium value at a unique rate, with the collision operator written in moment space as

$$\mathcal{C} = \mathbf{M}^{-1}\hat{\mathbf{S}}\left[\mathbf{m}_{\text{eq}}(\mathbf{x}_k, t_n) - \mathbf{m}(\mathbf{x}_k, t_n)\right]. \tag{1.50}$$

The moments relax toward their equilibrium values, denoted with the subscript "eq," at unique rates specified by the diagonal matrix $\hat{\mathbf{S}}$. A detailed account of the relaxation rates for porous medium flows is provided by Pan et al. [52]. The equilibrium value of the moments follows from this MRT formulation with additional terms present to account for surface forces, provided as follows:

$$m_{0\text{eq}} = \rho, \tag{1.51}$$

$$m_{1\text{eq}} = -11\rho + \frac{19}{\rho_0}\mathbf{j}\cdot\mathbf{j} - \sigma\,|\,\mathbf{C}\,|, \tag{1.52}$$

$$m_{2\text{eq}} = w_\epsilon \rho + \frac{w_{\epsilon j}}{\rho_0}\mathbf{j}\cdot\mathbf{j}, \tag{1.53}$$

$$m_{3\text{eq}} = j_x, \tag{1.54}$$

$$m_{4\text{eq}} = -\frac{2}{3}j_x, \tag{1.55}$$

$$m_{5\text{eq}} = j_y, \tag{1.56}$$

$$m_{6\text{eq}} = -\frac{2}{3} j_y, \tag{1.57}$$

$$m_{7\text{eq}} = j_z, \tag{1.58}$$

$$m_{8\text{eq}} = -\frac{2}{3} j_z, \tag{1.59}$$

$$m_{9\text{eq}} = \frac{1}{\rho_0}\left(2j_x^2 - j_y^2 - j_z^2\right) + \frac{1}{2}\sigma \,|\, \mathbf{C} \,|\, \mathbf{n}\cdot\mathbf{n}, \tag{1.60}$$

$$m_{10\text{eq}} = w_{xx} m_9, \tag{1.61}$$

$$m_{11\text{eq}} = \frac{1}{\rho_0}\left(j_y^2 + j_z^2\right) + \frac{1}{2}\sigma \,|\, \mathbf{C} \,|\left(n_y^2 - n_z^2\right), \tag{1.62}$$

$$m_{12\text{eq}} = w_{xx} m_{11}, \tag{1.63}$$

$$m_{13\text{eq}} = \frac{1}{\rho_0} j_x j_y + \frac{1}{2}\sigma \,|\, \mathbf{C} \,|\, n_x n_y, \tag{1.64}$$

$$m_{14\text{eq}} = \frac{1}{\rho_0} j_y j_z + \frac{1}{2}\sigma \,|\, \mathbf{C} \,|\, n_y n_z, \tag{1.65}$$

$$m_{15\text{eq}} = \frac{1}{\rho_0} j_x j_z + \frac{1}{2}\sigma \,|\, \mathbf{C} \,|\, n_x n_z, \tag{1.66}$$

$$m_{16\text{eq}} = 0, \tag{1.67}$$

$$m_{17\text{eq}} = 0, \tag{1.68}$$

and

$$m_{18\text{eq}} = 0. \tag{1.69}$$

The parameter σ is related linearly to the interfacial tension γ_{wn} [1]. The color gradient $\mathbf{C}$ and the associated unit normal vector $\mathbf{n}$ are computed from the nondimensional density field

$$\phi = \frac{\rho_w - \rho_n}{\rho_w + \rho_n}, \tag{1.70}$$

where ρ_w and ρ_n are obtained by solving a separate lattice Boltzmann equation that recovers the mass transport. The value of ϕ is constant in the bulk of each phase and varies within the transition

region in the fluid–fluid interface. Fluid–solid interactions (i.e., contact angle) are controlled by setting the value of ϕ to a constant value within the solid phase

$$\phi(\mathbf{x}_k) = \phi_s \quad \text{for } \mathbf{x}_k \in \Omega_s. \tag{1.71}$$

The color gradient is computed as

$$\mathbf{C} = \frac{3}{c_s^2 \delta_t} \sum_{i=0}^{N} w_i \mathbf{e}_i \phi(t, \mathbf{x}_k + \mathbf{e}_i \delta t), \tag{1.72}$$

and the unit normal vector is

$$\mathbf{n} = \frac{\mathbf{C}}{|\mathbf{C}|}. \tag{1.73}$$

A solution for the mass transport is provided by relying on a separate set of distributions to track the densities of the wetting and nonwetting phases, ρ_w and ρ_n, respectively. The associated distributions are computed based on these local density values, the flow velocity is determined from Equation 1.49, and the color gradient is determined from Equation 1.72. The distributions are determined by subjecting an equilibrium population to a recoloring step that minimizes the mass flux of each component in the direction of the color gradient. The redistribution step conserves the mass of each component exactly along with the total fluid momentum [41]

$$g_{iw} = w_i \left[\rho_w \left(1 + \frac{3}{c_s^2} \mathbf{e}_i \cdot \mathbf{u} \right) + \zeta \frac{\rho_w \rho_n}{\rho_w + \rho_n} \mathbf{n} \cdot \mathbf{e}_i \right], \tag{1.74}$$

and

$$g_{in} = w_i \left[\rho_n \left(1 + \frac{3}{c_s^2} \mathbf{e}_i \cdot \mathbf{u} \right) - \zeta \frac{\rho_w \rho_n}{\rho_w + \rho_n} \mathbf{n} \cdot \mathbf{e}_i \right]. \tag{1.75}$$

The parameter ζ determines the interfacial thickness, and the quadrature weights are

$$w_i = \begin{cases} \dfrac{1}{3}, & \text{for } q \in \{0\} \\ \dfrac{1}{18}, & \text{for } q \in \{1, 2, 3, 4, 5, 6\} \\ \dfrac{1}{36}, & \text{for } q \in \{7, 8, 9, 10, 11, 12, 13, 14, 15, 16, 17, 18\}. \end{cases} \tag{1.76}$$

The density values for the subsequent time step can then be computed as

$$\rho_\alpha(\mathbf{x}_k, t_n + \delta t) = \sum_{i=0}^{18} g_{i\alpha}(\mathbf{x}_k - \mathbf{e}_i \delta t, t_n) \quad \text{for } \alpha = w, n. \tag{1.77}$$

Combined with Equations 1.74 and 1.75, continuum expressions for mass conservation are thus obtained for each fluid component.

1.6.2 Verification and Parameter Estimation

The parameters that must be set in the LBM are ζ, which determines the width of the interface; σ, which controls interfacial tension; and the order parameter in the solid phase φ_s, which determines the contact angle. ζ was set to 0.9 based on previous analysis that confirmed the parameter is independent of interfacial tension and demonstrated there was no advantage to having a large interfacial thickness [46]. The parameters σ and φ_s were determined to match physical parameters of interest using a bubble test in the absence of a solid phase and a constrained bubble test in a capillary tube, respectively.

A 2D bubble test, in the absence of a solid phase, was used to measure the interfacial tension. A $40 \times 40 \times 3$ lattice was saturated with equal parts of wetting and nonwetting phases. Initially, a cylindrical shaped bubble of nonwetting phase with a defined radius was immersed in the wetting phase. Periodic boundary conditions were imposed in the x and y directions, with the z boundary being closed to flow. The system was allowed to progress to a steady state. When equilibrium was established, p_{wn} was measured as the difference in the pressure between the two phases. The values of p_n and p_w were extracted by using the phase indicator field to identify the maximum pressure value within each phase. The pressure maxima within each phase effectively excludes the interfacial region where small pressure fluctuations can occur.

In the bubble tests, equilibrium was defined when the change of dimensionless $p_n - p_w$ between time steps was less than 10^{-8}; it took approximately 40,000 time steps to achieve this criterion in the computational domain used. The difference in fluid pressures was related to the radius of curvature R through the 2D Young–Laplace equation given by

$$p_n - p_w = \frac{\gamma_{wn}}{R}. \tag{1.78}$$

Simulations for various bubble sizes were carried out, and the final radius of curvature R was calculated using imaging techniques detailed in the following text. The slope of the line relating the interfacial tension γ_{wn} and the parameter σ was found by plotting $p_n - p_w$ as a function of $1/R$ and fitting a linear function to the data points. In order to match the experimental interfacial tension, σ was determined to be 6.2×10^{-3}.

To control the contact angle with the LBM, the fluid–solid interactions with the solid phase were defined using a constrained bubble test suggested by Huang et al. [38]. In this case, a cylindrical capillary tube of radius R was used to provide a constraint on the equilibration of the bubble. With Equation 1.78 used to relate the interfacial curvature to the capillary pressure, the curvature was determined solely by the contact angle $\varphi_{ws,wn}$ between the wetting fluid–solid and wetting–nonwetting fluid interfaces according to

$$p_n - p_w = \frac{2\gamma_{wn}\cos\varphi_{ws,wn}}{R}. \tag{1.79}$$

Given the known value for σ from the previously described bubble test, the contact angle $\phi_{ws,wn}$ was determined by measuring the phase pressures and calculating $p_n - p_w$. Simulations in a capillary tube with a radius $R = 20$ were carried out for various values of ϕ_s and the corresponding $\phi_{ws,wn}$ values were calculated. The ϕ_s value that corresponded to the contact angle from a target physical system can thus be determined.

1.6.3 Validation

The computational expense required to simulate macroscale experiments has restricted the comparison of highly resolved microscale simulations with controlled experiments for two-fluid-phase flow. While some comparisons exist, virtually no comparisons exist that successfully compare these

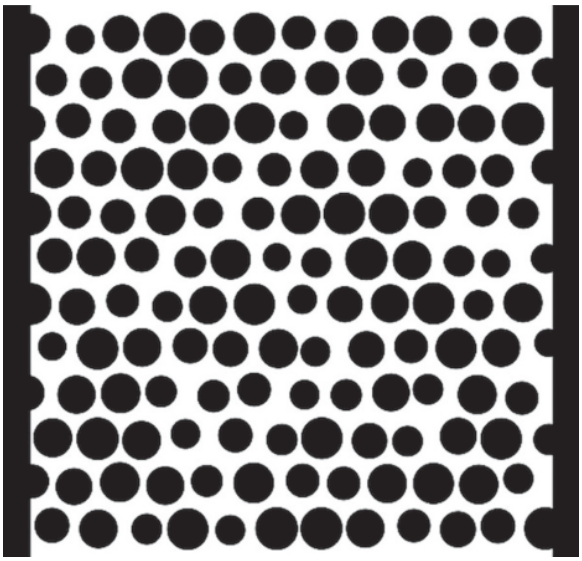

FIGURE 1.1 2D micromodel in which the solid is represented by black and the regions accessible to fluid flow by white.

systems for the full set of variables needed to close the TCAT model formulated earlier. Such comparisons of theory, experiment, and computation are a fruitful approach for advancing scientific understanding. To validate the LBM model, we performed a highly resolved microscale laboratory experiment and simulated this experiment using the LBM simulator with parameters determined for the contact angle and interfacial tension as described earlier.

The experimental methods follow the work of Pyrak-Nolte and coworkers [12]. A 2D micromodel consisting of a photosensitive polymer (photoresist) porous medium bounded by two glass slides was fabricated using lithographic methods and sealed into a cell that was 500 μm × 500 μm × 1.5 μm. Figure 1.1 is an illustration of the porous medium cell, which consisted of a distribution of cylinders with a porosity 0.52. In comparison to 3D systems, a higher porosity is necessary to ensure the connectivity of the pore space in a 2D cell. The cell was mounted horizontally on an optical microscope (Nikon SMZ-U Zoom 1:10) to avoid gravitational effects, and the microscope was interfaced to a CCD camera (Nikon D90). One outlet from the cell was connected to a wetting-fluid-phase decane reservoir, and a second outlet was connected to a nonwetting-fluid-phase nitrogen reservoir with individual and differential pressures measured using transducers (Omega PX319 and PX409). The other four boundaries of the cell were solid, no-flow boundaries. The contact angle of the decane with the photoresist material and the decane–nitrogen gas interfacial tension were measured to be 4.1° and 24.7 dynes/cm, respectively [12]. The experiment was conducted in an ultraviolet-free room with temperature maintained constant at 24°C.

A displacement experiment was performed by fully saturating the porous medium region of the cell with decane through the inlet reservoir. Primary drainage of the cell was accomplished by increasing the pressure of the nitrogen reservoir such that an increasing portion of the decane was displaced over a series of discrete pressure steps. After each pressure step, the system was allowed to equilibrate, and an image of the system and the final pressures were recorded. A series of steps leading to decane imbibition followed a partial primary drainage sequence. Following drainage, an imbibition sequence was studied by decreasing the nitrogen pressure, allowing decane to imbibe back into the cell. The experimental results are shown in Figure 1.2.

A 2D LBM simulation of the drainage and imbibition sequence was performed matching experimental conditions with a 0.5 μm grid resolution, and the computational results are also shown in Figure 1.2. In the LBM simulations, the experimental conditions were mimicked by setting a

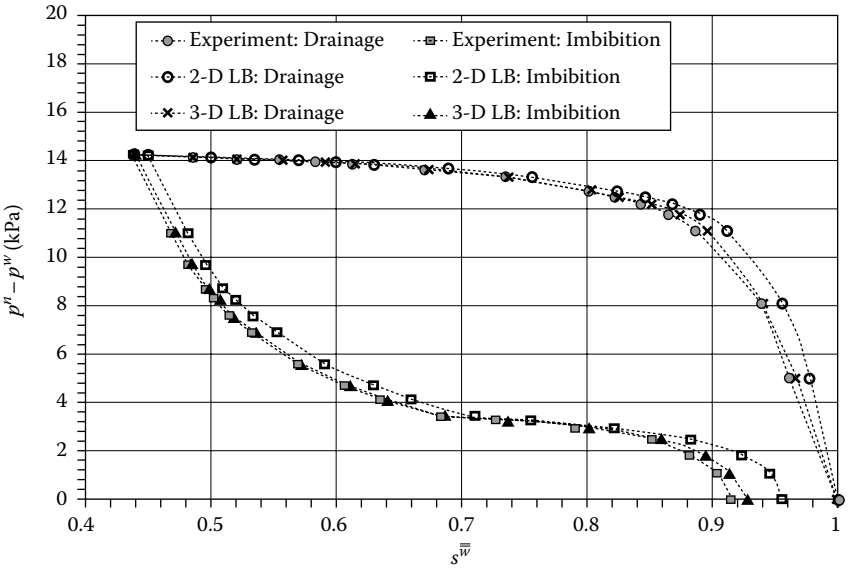

FIGURE 1.2 Pressure–saturation curves obtained from the displacement experiment and the LBM simulations for the porous geometry shown in Figure 1.1.

constant pressure boundary condition on one inlet face for one fluid and on the other inlet face for the second fluid and setting no-flow boundaries for all other horizontal boundaries. The 3D simulator employed was reduced effectively to two dimensions by having only one interior grid block in the vertical dimension and periodic boundaries in this dimension. The pressure boundary conditions for the LBM simulation were determined by scaling the external pressure applied in the experimental system using the Young–Laplace equation, Equation 1.78, to give

$$\frac{(p_n - p_w)}{\gamma_{wn}} - \frac{1}{R_z} = \frac{p_{nLB} - p_{wLB}}{D\gamma_{wnLB}}, \tag{1.80}$$

where

$p_n - p_w$ is the pressure difference between the two first-kind boundary conditions for the fluids in the cell obtained from the pressure transducer reading
γ_{wn} is the decane–nitrogen interfacial tension (24 dynes/cm)
R_z is the principal radius of curvature in the z direction
D is the lattice resolution (0.5 μm per lattice unit)
LB denotes a value in the LBM model

The lattice spacing D is introduced to scale the dimensionless LBM variables. Note that since the experiments have curvature in the z direction and the 2D simulations do not, the radius of curvature in the vertical dimension, R_z, had to be subtracted from the $p_n - p_w$ value obtained from the experimental system. This reduction of dimensionality can be viewed as an assumption that the curvature in the vertical dimension of the experimental cell is always in an equilibrium state. Given the short length scale in the vertical dimension, this approach seems reasonable.

The experimental and simulated results shown in Figure 1.2 have similar shapes with simulated saturations at a given $p_n - p_w$ typically within a few percent of the experimentally observed values. Reasons for the differences between the simulated and observed results include the following possible sources of error: potential variations in the shape of the cylindrical features that make up the porous medium with depth due to overexposure or underexposure during fabrication,

the representation of the smooth cylindrical features of the experiment with a fixed-grid discrete lattice that is inherently jagged, the use of literature values for the contact angle and interfacial tension, pressure transducer and image analysis errors, and the use of a 2D simulation to approximate a 3D experiment. To further investigate the potential sources of error between the experimental results and the LBM simulations, a 3D LBM model was used to simulate conditions, including the vertical boundary conditions, consistent with the experiments using a grid resolution of 0.25 μm in the x–y plane and 0.015 μm in the z dimension. Figure 1.2 shows that the more highly resolved 3D LBM simulation more closely represents the experimental data than the less highly resolved 2D simulation. Part of this difference is likely due to a more accurate representation of the cylindrical solid phase with an improved grid resolution. Given the known and potential sources of error, the agreement between the experimental data and the LBM simulations is judged to be acceptable and a sufficient validation of the LBM simulator to be used for the purpose of evaluating TCAT closure relations.

1.7 COMPUTATIONAL GEOMETRY METHODS

The computation of variables appearing in TCAT models requires the evaluation and integration of data from experimental observations or microscale simulations. In general, these approaches rely on three main components:

1. A sufficiently resolved source of microscale information, which may be obtained from a computational simulation or from images of an experimental system
2. A framework to numerically approximate each of the entity domains and their boundaries, including phases, interfaces, and common curves
3. A means to approximate macroscale averages based upon the underlying microscale representation of the experimental or simulated system

The regular lattice used for the LBM provides a natural way to evaluate the volumetric averages, with the dimensionless density field ϕ identifying the regions of space occupied by either phase. For the images of experimental systems, the phase positions are extracted by smoothing the image using a median filter, then selecting an isovalue that segments the pore space between wetting and nonwetting phases. This isovalue also defines the interface between the wetting and nonwetting fluids. The position of the solid phase is known, which allows all phases and interfaces to be identified explicitly. Given this information, TCAT averages can be determined in an analogous fashion for both the experimental and simulated data.

To perform averaging over an interface or a common curve, a numerical approximation must be constructed for each of these entities. The porous medium marching cubes algorithm was used to approximate Ω_{wn}, Ω_{ws}, Ω_{ns}, and Ω_{wns} [45]. For the interfaces, lists of triangles were constructed to represent each entity. Line segments that approximate the common curve were extracted at the intersection of the three surfaces. Microscale quantities were then interpolated to points on the interfaces or common curve and averaged using quadrature methods to match the respective TCAT definition of each variable. For the experimental images, a 2D analog of this approach was developed to extract the interfaces present in the system and evaluate the interfacial curvature.

1.8 TCAT CLOSURE RELATIONS

1.8.1 Simulations

The verified and validated LBM model was used to evaluate the closure relations needed for the TCAT two-fluid-phase model. Specifically, relations among fluid pressures, saturations, interfacial areas, curvatures, and dynamic evolution equations as described by Equations 1.39 through 1.43

were sought. The basic notion here is that we have shown that the 2D LBM can simulate with reasonable accuracy the 3D micromodel experiments. Since the micromodel is a valid porous medium system, we have a means to compute the detail needed to address TCAT closure relations. Although not strictly necessary, reducing the model to two dimensions greatly decreased the computational burden. Highly resolved 3D simulations would have provided a more accurate representation of the model system.

LBM simulations of drainage and imbibition were performed to mimic the micromodel experiment used to validate the model. The initial condition was a fully wetting-phase-saturated system. The simulated boundary conditions were

$$p^w(0, y, z, t) = p_b^w(t), \tag{1.81}$$

$$p^n(x_l, y, z, t) = p_b^n(t), \tag{1.82}$$

$$\left.\frac{\partial p^n}{\partial x}\right|_{0,y,z,t} = 0 \tag{1.83}$$

and

$$\left.\frac{\partial p^w}{\partial x}\right|_{x_l,y,z,t} = 0, \tag{1.84}$$

where

x_l is the length of the domain in the x direction

the subscript b denotes a boundary value, and periodic boundary conditions were used in the y and z dimensions

These conditions ensured that the wetting fluid and the nonwetting fluid entered and exited one face of the domain, matching the manner in which traditional laboratory experiments are performed. The boundary conditions were adjusted in discrete jumps in time and the simulator was run until an equilibrium state was approached, observing both the final approximate equilibrium state and the dynamics of the approach to the approximate equilibrium state. True equilibrium states were not simulated because interfacial curvature relaxation was not monitored and used as a termination criterion in the simulations. Termination was based upon a small change in fluid saturations. True equilibrium requires longer to achieve beyond the point at which fluid saturations changes are small. The LBM results were averaged over the domain, and these results were used to produce the macroscale quantities of interest in TCAT model closure.

A sequence of pressure boundary conditions was set to simulate primary drainage, main imbibition, and both imbibition and drainage scanning curves. Primary drainage was simulated until an asymptotic wetting-phase saturation was approached; main imbibition was simulated until a state where the boundary conditions were $p^n = p^w$. Figure 1.3 depicts the set of equilibrium states that were simulated, while the curves passing through the points indicate the sequence of the simulations used to reach a given equilibrium state. As was the case with the micromodel validation experiment, imbibition resulted in the formation of a disconnected, entrapped residual nonwetting phase. Examples of the simulated fluid displacement patterns for both primary drainage and main imbibition are depicted in Figures 1.4 and 1.5, respectively. The residual nonwetting phase is clearly shown

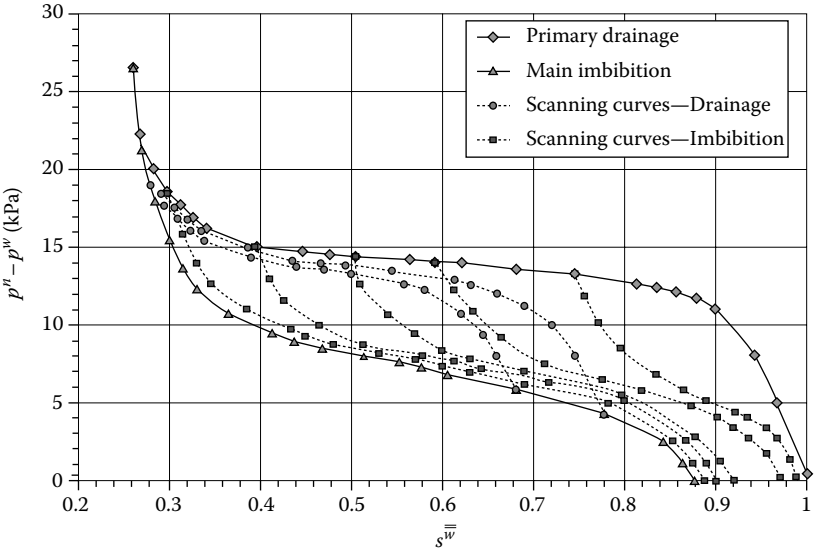

FIGURE 1.3 Pressure–saturation quasi-equilibrium states computed using the LBM.

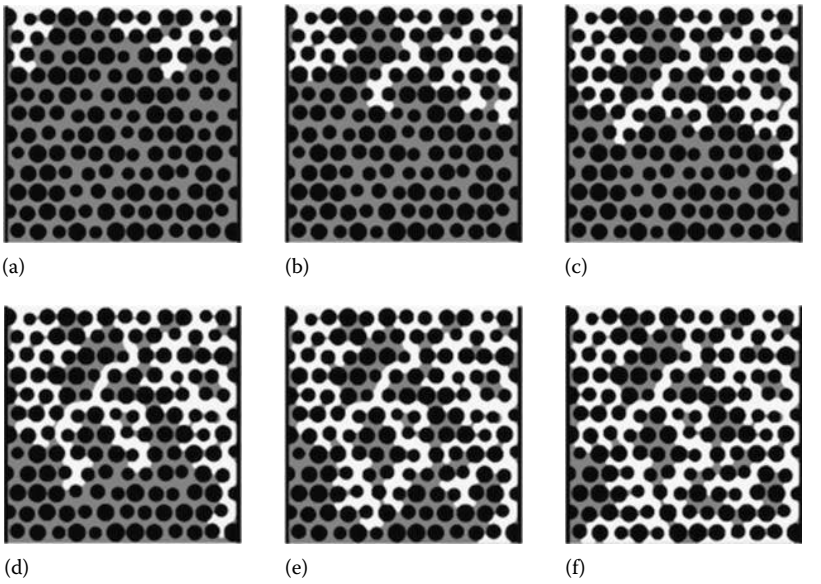

FIGURE 1.4 Fluid distributions for a set of equilibrium states along the simulated primary drainage curve shown in Figure 1.3. Black represents the solid phase, white represents the nonwetting fluid phase, and gray represents the wetting fluid phase. (a) $s^{\overline{\overline{w}}} = 0.85$, (b) $s^{\overline{\overline{w}}} = 0.709$, (c) $s^{\overline{\overline{w}}} = 0.598$, (d) $s^{\overline{\overline{w}}} = 0.482$, (e) $s^{\overline{\overline{w}}} = 0.383$, (f) $s^{\overline{\overline{w}}} = 0.272$.

by the set of disconnected nonwetting-phase (DNP) regions that remain after imbibition is complete. Each of these discrete nonwetting-phase regions formed under specific fluid pressure conditions. Therefore, each residual region at equilibrium has a distinct curvature, corresponding to a capillary pressure that was established at the time the disconnected region was formed. This observation has implications for modeling and model closure.

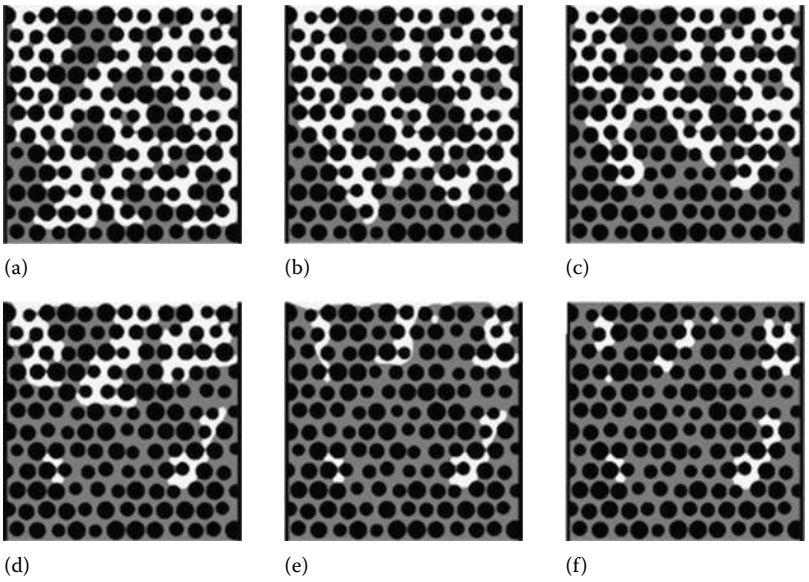

FIGURE 1.5 Fluid distributions for a set of equilibrium states along the simulated main imbibition curve shown in Figure 1.3. Black represents the solid phase, green represents the nonwetting fluid phase, and blue represents the wetting fluid phase. (a) $s^{\overline{\overline{w}}} = 0.356$, (b) $s^{\overline{\overline{w}}} = 0.43$, (c) $s^{\overline{\overline{w}}} = 0.52$, (d) $s^{\overline{\overline{w}}} = 0.705$, (e) $s^{\overline{\overline{w}}} = 0.855$, (f) $s^{\overline{\overline{w}}} = 0.895$.

1.8.2 Capillary Pressure–Saturation–Interfacial Area Relation

Traditional two-phase-flow models are closed using hysteretic pressure–saturation relations that account for nonwetting fluid entrapment but do not explicitly account for variables known from pore-scale analysis to be important, such as interfacial tensions, interfacial curvatures, and contact angles [48]. The nature of two-fluid-phase porous medium systems also suggests interfacial areas are important. The absence of important variables in closure relations for traditional models and the hysteretic nature of these relations are indicators of a modeling approach in which underlying physics has been relegated to implicit parameterization. The TCAT model formulated to describe two-fluid-phase flow posits general functional forms of closure relations that explicitly include the traditionally neglected variables. As previously noted, the determination of specific forms of these relations is an active area of current and recent research. The LBM simulations summarized earlier provide a means to investigate these closure relations with an ultimate goal being to determine specific functional forms that represent the behavior of the system.

The simulated quasi-equilibrium points were analyzed to determine the fluid pressures, p^w and p^n; the average curvature, J_w^{wn}; the saturation of the wetting phase, $s^{\overline{\overline{w}}}$; and the specific interfacial area, $\epsilon^{\overline{\overline{wn}}}$. Various subsets of the entire data set were examined to gain insight into the nature of the relation sought. In addition, subsets of the data excluding the DNP fluid were also considered. By DNP, we mean that a continuous connection to the Dirichlet boundary corresponding to the nonwetting phase cannot be traced through the system. Note that this definition implicitly has a length scale associated with it, and we take this length scale to be that associated with the averaging region over which the TCAT model is developed. Figure 1.5 shows cases in which a DNP forms during main imbibition. The goals of these simulations were to determine in a semiquantitative manner if the inclusion of interfacial area can remove the hysteresis associated with traditional models, to evaluate the role of the DNP, and to evaluate the nature of the dynamic rate of relaxation to an equilibrium state.

The data shown in Figure 1.3 were processed using the image analysis approaches described in §7 to determine the TCAT variables of interest. To close the TCAT model formulated, consistent equations of state are needed for Equations 1.40 and 1.41. Because we know that at equilibrium $p^{wn} = p^n - p^w$, a single, smooth invertible function could provide the closure information needed. Simulation results confirmed that this condition is reasonable, within a small error associated with the estimation of the curvature. The issue thus becomes identifying the necessary function from the data available or at least determining if such a well-behaved function is likely to exist given the data available. The desired function would fit the entire data set, including all scanning curves, and be single valued, and thus nonhysteretic. The pooled data for the primary drainage, main imbibition, and all scanning curves were examined for the cases in which the DNP fluid was included with the nonwetting phase fluid and for the case in which the DNP fluid was excluded. By inclusion and exclusion of the DNP, we mean that $s^{\bar{\bar{w}}}$ and $\epsilon^{\bar{\bar{wn}}}$ were computed including either all of the nonwetting phase or only the continuous, connected portion of the nonwetting phase.

A polynomial function proposed to have the form

$$\epsilon^{\bar{\bar{wn}}} + b_0 p^{(wn)^2} + p_1 s^{\bar{\bar{w}}^2} + b_2 p^{wn} s^{\bar{\bar{w}}} + b_3 p^{wn} + b_4 s^{\bar{\bar{w}}} + b_5 = 0 \tag{1.85}$$

was fit to all of the data shown in Figure 1.3 using nonlinear least squares for the cases with and without the inclusion of DNP in the computation of $s^{\bar{\bar{w}}}$ and $\epsilon^{\bar{\bar{wn}}}$. The minimized root-mean-square error between the estimated function and the data was computed according to

$$\varepsilon_{RMSE} = \sqrt{\frac{1}{3n}\sum_{i=1,n}\left[\left(\frac{p^{wni} - p^{wni*}}{p^{wn}_{\max} - p^{wn}_{\min}}\right)^2 + \left(\frac{\epsilon^{\bar{\bar{wni}}} - \epsilon^{\bar{\bar{wni*}}}}{\epsilon^{\bar{\bar{wn}}}_{\max} - \epsilon^{\bar{\bar{wn}}}_{\min}}\right)^2 + \left(\frac{s^{\bar{\bar{w}}i} - s^{\bar{\bar{w}}i*}}{s^{\bar{\bar{w}}}_{\max} - s^{\bar{\bar{w}}}_{\min}}\right)^2\right]}. \tag{1.86}$$

Additionally, the mean normalized error was calculated as

$$\varepsilon_{MAE} = \frac{1}{3n}\sum_{i=1,n}\left[\frac{\left|p^{wni} - p^{wni*}\right|}{p^{wn}_{\max} - p^{wn}_{\min}} + \frac{\left|\epsilon^{\bar{\bar{wni}}} - \epsilon^{\bar{\bar{wni*}}}\right|}{\epsilon^{\bar{\bar{wn}}}_{\max} - \epsilon^{\bar{\bar{wn}}}_{\min}} + \frac{\left|s^{\bar{\bar{w}}i} - s^{\bar{\bar{w}}i*}\right|}{s^{\bar{\bar{w}}}_{\max} - s^{\bar{\bar{w}}}_{\min}}\right]. \tag{1.87}$$

In these expressions, the sum of errors for each of the variables was computed by specifying the other two variables from the set of p^{wn}, $\epsilon^{\bar{\bar{wn}}}$, and $s^{\bar{\bar{w}}}$ and computing the root from Equation 1.85 to determine the third value; max denotes the maximum value; min denotes the minimum value; i is a data point index; n is the total number of data points in the set; and * denotes the functional value fit using Equation 1.85. Normalization of the variables was performed to rescale all the variables to a common range of [0, 1].

Nonlinear least squares yielded the coefficients tabulated in Table 1.1, and the corresponding errors are listed in Table 1.2. These results show that a simple quadratic function represents the

TABLE 1.1
Best-Fit Coefficients for Functional Form Given by Equation 1.85

	b_0	b_1	b_2	b_3	b_4	b_5
Inclusion of DNP	-1.67×10^{-5}	0.0108	−0.0011	0.0013	0.0297	−0.0398
Exclusion of DNP	-2.14×10^{-5}	0.0010	−0.0010	0.0015	0.0344	−0.0434

TABLE 1.2
Normalized Errors for Estimation of Variables Given Functional Fits Corresponding to the Coefficients Listed in Table 1.1

	$p^{wn} = p^{wn}\left(s^{\bar{\bar{w}}}, \epsilon^{\bar{\bar{wn}}}\right)$		$\epsilon^{\bar{\bar{wn}}} = \epsilon^{\bar{\bar{wn}}}\left(p^{wn}, s^{\bar{\bar{w}}}\right)$	
	ε_{RMSE}	ε_{MAE}	ε_{RMSE}	ε_{MAE}
Inclusion of DNP	0.045	0.031	0.045	0.032
Exclusion of DNP	0.031	0.022	0.028	0.015

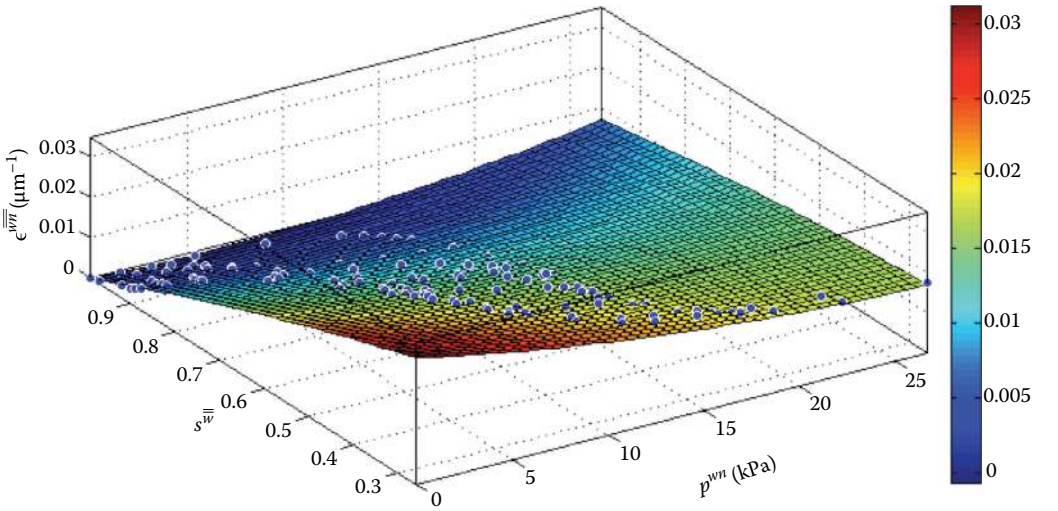

FIGURE 1.6 $\epsilon^{\bar{\bar{wn}}}$ as a function of p^{wn} and $s^{\bar{\bar{w}}}$ for the case in which DNP is excluded.

data reasonably well and that errors are reduced by excluding DNP from the fits. The surface fit to the data is shown in Figure 1.6 for the case in which DNP is removed from the analysis. The results also show that the function determined is invertible and thus hysteresis is essentially eliminated. To further demonstrate properties of the equation of state, determined for the case with DNP excluded, the relationship between the observed and predicted values of $s^{\bar{\bar{w}}}$ is shown in Figure 1.7. This figure demonstrates that the equation of state is an accurate representation of the LBM simulations.

1.8.3 Disconnected Nonwetting Phase

Results from the previous section illustrated that DNP plays an important role in the behavior of two-fluid-phase flow systems. It is important to identify this portion of the n phase and account for it appropriately in the model closure. This observation is consistent with the treatment of the nonwetting phase in traditional two-fluid-phase flow models [36,48,63], where typically some linear or nonlinear model of the fluid saturations is used to approximate the DNP. The importance of treating the DNP differently from the connected nonwetting phase was shown as a result of the equation of state fitting in the previous section, and it also seems reasonable based upon physical reasoning. Because the LBM simulations provide complete microscale detail of the fluid

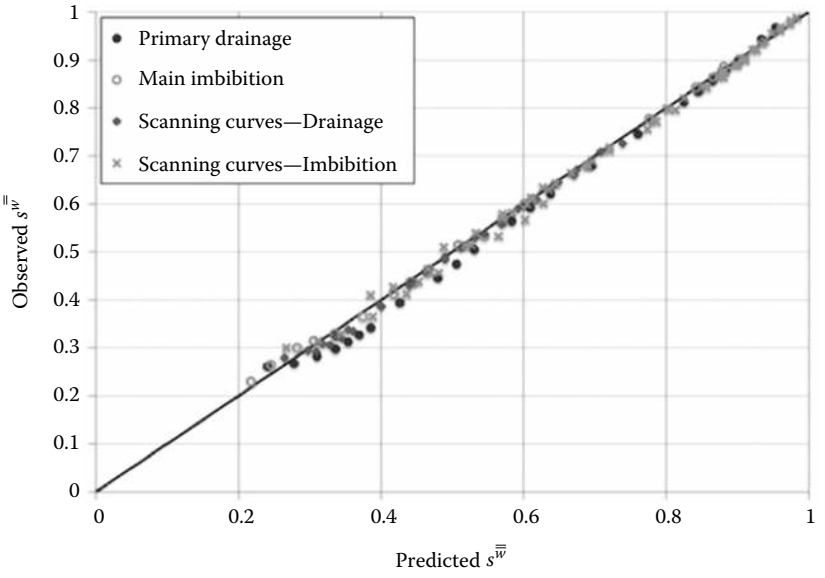

FIGURE 1.7 Error in $s^{\bar{\bar{w}}}$ resulting from the equation of state given by Equation 1.85 for the case in which DNP is excluded.

distributions, some details of the DNP are accessible based upon the simulations. For example, the saturations, curvatures, interfacial area, and geometric orientation tensor distribution of all DNP regions are available. Such information would not typically be available from traditional macroscale laboratory experiments, and it is also burdensome to collect such data even for high-resolution imaging methods because of the number of discrete equilibrium points needed to understand the formation of DNP.

We examined two aspects of DNP residual formation: (1) the maximum volume of DNP that can be formed for a given system, which occurs at $p^{wn} = 0$, along with identification of the variable(s) that enable the approximation of this formation potential, and (2) the amount of DNP at any quasi-equilibrium state. During primary drainage the nonwetting phase is connected to the boundary and thus DNP does not form. However, once imbibition starts from any partially drained state, DNP can begin to form due to snap off of the nonwetting phase. The usual case is to posit that the maximum DNP that can form in a system is a function of the minimum wetting-phase saturation that is achieved. Mechanistically, this means that the greater the fraction of the pore space that is accessed by the nonwetting phase at some point, the greater the potential to form DNP as imbibition occurs. The maximum DNP forms at the completion of the main imbibition stage, and the magnitude of this quantity depends upon the pore morphology and topology as well as the properties of the fluids and the solid. Because we have only examined a single system, pore morphology and topology factors were not evaluated in this work.

As part of the examination of the maximum DNP formation capacity, Figure 1.8 shows the relationship between the minimum wetting-phase saturation state of a system at any point in time and the maximum DNP that forms when $p^{wn} = 0$. The main imbibition and all imbibition-scanning curves were used to create this figure. These data show that a relatively smooth, monotonic, and nonlinear relationship exists between these two variables. Note that the shape is constrained by zero DNP as minimum $s^{\bar{\bar{w}}}$ approaches unity and a maximum attainable value of DNP as the minimum value of $s^{\bar{\bar{w}}}$ approaches the irreducible wetting-phase saturation. This curvilinear form is consistent with established methods of describing the DNP formation capacity [36]. Additional data could be

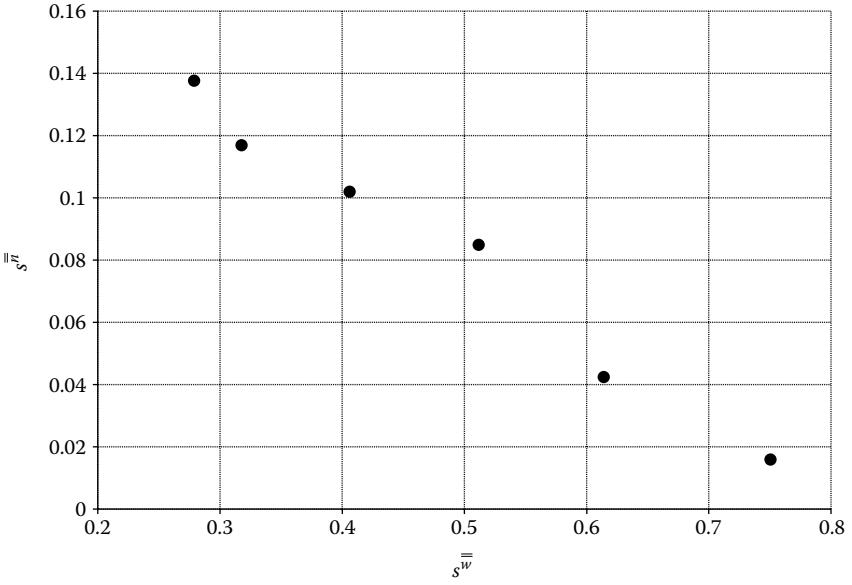

FIGURE 1.8 Maximum DNP saturation that can form as a function of the minimum wetting-phase saturation state of the system.

used to further refine this relationship, but the available data support the suggested parameterization of this relation as a function that depends upon the minimum value of $s^{\overline{\overline{w}}}$.

The second aspect of DNP is the estimation of the quantity for any equilibrium state of the system. Given the observations made earlier, two limits can be noted for any system. The lower limit is

$$\lim_{s^{\overline{\overline{w}}} \to s^{\overline{\overline{w,\min}}}} s^{\overline{\overline{nd}}} = 0, \tag{1.88}$$

and the upper limit is

$$\lim_{p^n - p^w \to 0} s^{\overline{\overline{nd}}} = s^{\overline{\overline{nd,\max}}}, \tag{1.89}$$

where

$s^{\overline{\overline{nd}}}$ is the saturation of the DNP
min denotes a minimum value
max denotes a maximum value

Equation 1.88 is consistent with the notion that DNP does not exist during primary drainage and a requirement that imbibition scanning curves that are reversed will be closed at the point of departure from the primary drainage curve, and Equation 1.89 is the definition of the maximum DNP. The most appropriate function to describe the DNP at intermediate saturations will depend upon characteristics of the morphology and topology of the pore space.

A remaining DNP issue that has not received attention in the literature is elucidation of the dynamics of the formation of DNP. It seems reasonable that if the dynamics of fluid saturations,

pressures, and interfacial areas are important and that DNP must be accounted for, then the dynamics of the formation and destruction of DNP must also be modeled. No method has been advanced to account for this phenomenon in a TCAT-based two-fluid-phase flow model.

1.8.4 Dynamic Relaxation

The TCAT model for two-fluid phases formulated in §4 includes dynamic changes in the relationship among capillary pressure, fluid saturations, and interfacial areas. This model formulation makes use of a general form of a state equation for capillary pressure given as Equation 1.39, a general form of an equilibrium relationship for interfacial area given by Equation 1.41, and a dynamic equation that expresses the relaxation of fluid pressures, capillary pressure, fluid saturation, and interfacial area to an equilibrium state. Because this formulation is new, aspects of this general formulation need further development and evaluation.

Consider the state equation for capillary pressure and the equilibrium relationship for interfacial area, which are restated as

$$p^{wn} = p^{wn}\left(s^{\bar{\bar{w}}}, \epsilon^{\bar{\bar{wn}}}\right) \tag{1.90}$$

and

$$\epsilon^{\bar{\bar{wn}}}_{\mathrm{eq}} = \epsilon^{\bar{\bar{wn}}}_{\mathrm{eq}}\left(p^n - p^w, s^{\bar{\bar{w}}}\right). \tag{1.91}$$

Pore-scale simulations have been used to deduce an approximate form of Equation 1.90. This smooth function can be inverted to determine $\epsilon^{\bar{\bar{wn}}}$ as a function of p^{wn} and $s^{\bar{\bar{w}}}$; alternatively a smooth quadratic function can be fit to the data to represent this inverted quantity saving the issue of multiple roots. This equation has the form

$$\epsilon^{\bar{\bar{wn}}} = F\left(p^{wn}, s^{\bar{\bar{w}}}\right). \tag{1.92}$$

When the system is not at equilibrium, we can identify an expected value of $\epsilon^{\bar{\bar{wn}}}$ that would exist if the system were at equilibrium as

$$\epsilon^{\bar{\bar{wn}}}_{\mathrm{eq}} = F\left(p^n - p^w, s^{\bar{\bar{w}}}\right). \tag{1.93}$$

It can be shown that at equilibrium,

$$p^{wn} = p^n - p^w. \tag{1.94}$$

Therefore, the difference between $\epsilon^{\bar{\bar{wn}}}$ and $\epsilon^{\bar{\bar{wn}}}_{\mathrm{eq}}$ is a measure of disequilibrium and is employed in Equation 1.30 as a driving force for evolution of the interfacial area toward equilibrium.

To evaluate the validity of Equation 1.90 as a state equation, we extracted the data from a dynamic portion of the LBM simulations as the system relaxed to an equilibrium state and compared the p^{wn} predicted by the state equation with the p^{wn} that was observed in the dynamic simulations. The results shown in Figure 1.9 demonstrate a good agreement between the capillary pressure obtained under dynamic conditions in the simulations and predictions based upon the state equation derived

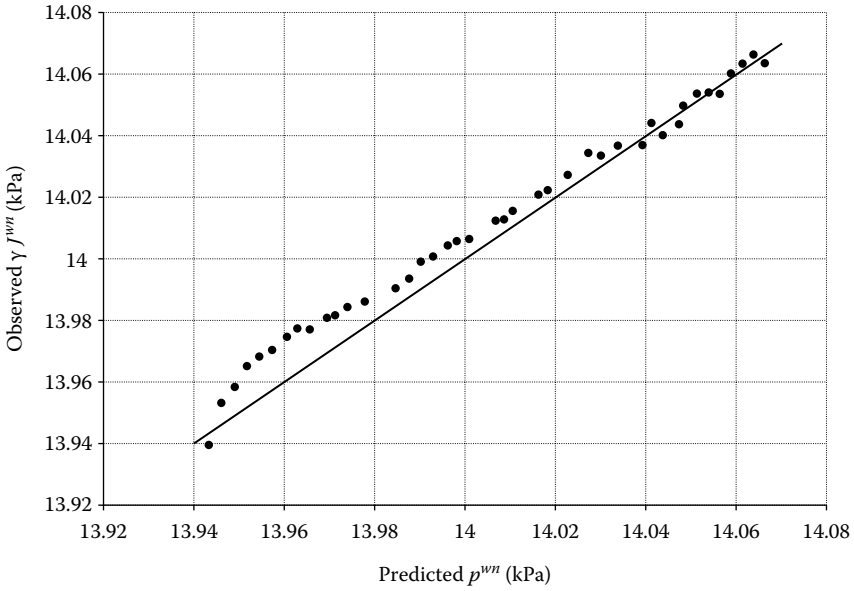

FIGURE 1.9 Observed versus predicted values of p^{wn} for points from a dynamic LBM simulation of relaxation to an equilibrium state.

using only the quasi-equilibrium data. It seems possible that the general state equation could be further improved by including not only equilibrium data but also dynamic data in its formulation. In other words, the simple quadratic form employed in this work, Equation 1.85, can likely be improved upon, but the results are encouraging in the context of the model formulation that has been proposed.

Equation 1.33 can be restated as

$$p^n - p^w = p^{wn} - \frac{\epsilon}{\hat{c}^{wn}} \frac{\partial s^{\overline{\overline{w}}}}{\partial t} + \frac{\gamma^{wn} \hat{k}_1^{wn} \left(\epsilon^{\overline{\overline{wn}}} - \epsilon_{\text{eq}}^{\overline{\overline{wn}}} \right)}{\hat{c}^{wn} \left(p^w - p^n \right)}. \tag{1.95}$$

Because the LBM simulations yield dynamic information of the relaxation to an equilibrium state, these simulations can be used to determine $\hat{c}^{wn}$ and $\hat{k}_1^{wn}$ and to evaluate how well Equation 1.95 represents the simulated system. To accomplish these goals, Equation 1.95 was written as

$$\varepsilon_{\text{dyn}} = p^n - p^w - p^{wn} + \frac{\epsilon}{\hat{c}^{wn}} \frac{\partial s^{\overline{\overline{w}}}}{\partial t} - \frac{\gamma^{wn} \hat{k}_1^{wn} \left(\epsilon^{\overline{\overline{wn}}} - \epsilon_{eq}^{\overline{\overline{wn}}} \right)}{\hat{c}^{wn} \left(p^w - p^n \right)}. \tag{1.96}$$

Then, ε_{dyn} was minimized in a least squares sense to determine $\hat{c}^{wn}$ and $\hat{k}_1^{wn}$ using cubic spline representations of all other quantities derived from the LBM simulations. The value of various groupings of terms from this equation is shown in Figure 1.10. The dynamic approach to equilibrium was represented well by Equation 1.95, and the three groupings of terms show that all components of this equation are important. It is especially telling that the interfacial area term is relatively large compared to the temporal derivative of $s^{\overline{\overline{w}}}$, because the interfacial area term has not been included in other so-called dynamic capillary pressure models, suggesting that important physics has been overlooked in these alternative approaches.

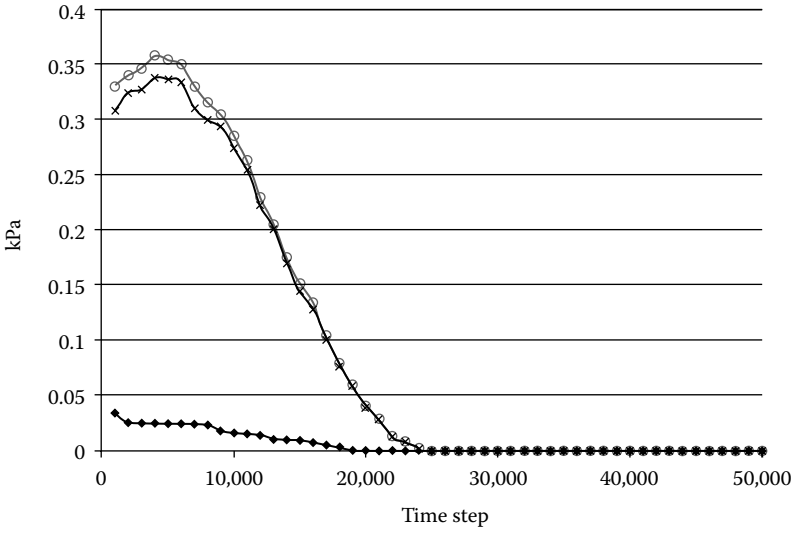

FIGURE 1.10 The line passing through the circles is the term $p^n - p^w - p^{wn}$, the line crossing through the x symbols is the term involving the interfacial area in Equation (1.96), and the line crossing through the diamonds is the term involving the temporal derivative of saturation in Equation (1.96).

1.9 DISCUSSION AND CONCLUSIONS

The elements of the TCAT theory have been summarized and used to formulate a two-fluid-phase flow model. The formulated model has many attractive features including connection across scales, a sound thermodynamic basis, inclusion of relevant physics missing from traditional models, and general forms of all closure relations needed to produce a solvable model. Because the formulated TCAT model is new and the closure relations have not yet been deduced in a specific and refined functional form, significant work remains to produce a solvable TCAT model.

Microscale simulation methods have matured to the point that they can be used to provide the sort of high-resolution simulations needed to formulate meaningful closure relations. The microscale detail from such simulations can be averaged to determine the various TCAT quantities that emerge from the model formulation. An LBM method was advanced that is capable of providing the sort of information needed to produce the closure relations sought for the formulated TCAT model. This simulator was validated by comparing to micromodel experiments, which are more costly and time consuming to perform than the desired simulations. Thus, simulation was used as a basis to investigate the closure relations sought.

Support was provided for the existence of a smooth, invertible, and unique relationship among capillary pressure, fluid saturation, and interfacial area between the fluid phases. Simulation results revealed that a simple quadratic function represented the data more accurately when the DNP was excluded from the analysis. This observation is reasonable because individual regions of DNP form over a range of capillary pressures. It seems consistent, then, to formulate and solve models that account explicitly for DNP. Such a TCAT model has not been formulated. Aspects of DNP that are important include the maximum amount that can form in a system, the amount formed under equilibrium conditions at any state point, and the role of dynamics in the formation and destruction of DNP. Significant opportunities for future work exist in these open areas of knowledge.

The LBM data were used to probe the posited dynamic form of the model. These efforts revealed an encouraging level of agreement between the posited evolution equation and microscale observations. It appears that a local equilibrium–based state equation can describe the nonequilibrium data. Also of significant interest is the importance of the deviation from equilibrium of the interfacial area state as an important component in relaxation of fluid pressures to the capillary pressure at

equilibrium. The importance of this interfacial area term has not been shown in the literature; other evolving multiphase models only include the change in fluid saturation in posited forms of a non-equilibrium equation for capillary pressure.

NOMENCLATURE

b	entropy body source density
$\mathbf{C}$	Green's deformation tensor, $\nabla_X \mathbf{x} \cdot (\nabla_X \mathbf{x})^{\mathrm{T}}$
$\mathbf{C}^s$	macroscale Green's deformation tensor, $\left\langle \mathbf{C}_s \right\rangle_{\Omega_s, \Omega_s}$
$\mathbf{C}$	constant velocity vector
$\mathbf{C}$	gradient of the dimensionless density field/color gradient
$\mathcal{C}_i$	collision operator for the LBM
$\hat{c}$	closure coefficient
c_s	speed of sound
$\mathbf{d}^{\bar{\bar{\alpha}}}$	macroscale rate of strain tensor, $[\nabla \mathbf{v}^{\bar{\alpha}} + (\nabla \mathbf{v}^{\bar{\alpha}})^{\mathrm{T}}]/2$
E	internal energy density
$E^{\bar{\bar{\alpha}}}$	macroscale energy of entity α per total volume, $\left\langle E_\alpha \right\rangle_{\Omega_\alpha, \Omega}$
$\mathcal{E}_*^{\bar{\bar{\alpha}}}$	particular material derivative form of a macroscale entity total energy conservation equation
$\mathcal{E}_d$	set of discrete velocity vectors
$\mathbf{e}_i$	discrete velocity vector i
f	general scalar function
$\mathbf{f}$	vector containing discrete distributions for the LBM
$\mathcal{F}_{dk}$	set of discrete distributions
$\mathbf{G}^\alpha$	macroscale orientation tensor for α interface or common curve, $\left\langle \mathbf{I} - \mathbf{I}_\alpha^{(n)} \right\rangle_{\Omega_\alpha, \Omega_\alpha}$
$\mathcal{G}_*^{\bar{\bar{i\alpha}}}$	particular material derivative form of a macroscale species-based body force potential balance equation
$\mathcal{G}_*^{\bar{\bar{\alpha}}}$	particular material derivative form of a macroscale entity-based body force potential balance equation
$\mathbf{g}$	body force per unit mass, acceleration
g_i^α	LBM distribution for mass transport of phase α
h	energy source density
h^α	macroscale energy source density for entity α
$\mathbf{I}$	unit tensor
$\mathbf{I}_\alpha^{(n)}$	unit tensor associated with 3 – n-dimensional entity, α, where (n) is the number of primes used
$\mathbf{J}$	set of entity indices
$\mathcal{J}_{c\alpha}$	connected set of indices for entity α, $= \mathcal{J}_{c\alpha}^+ \cup \mathcal{J}_{c\alpha}^-$
$\mathcal{J}_{c\alpha}^+$	connected set of indices of dimension higher than entity α
$\mathcal{J}_{c\alpha}^-$	connected set of indices of dimension lower than entity α
$\mathcal{J}_{\mathrm{f}}$	set of fluid-phase indices
$\mathcal{J}_{\mathrm{I}}$	set of interface indices
$\mathcal{J}_{\mathrm{P}}$	set of phase indices
$\mathcal{J}_{\setminus s}$	set of entity indices except the solid phase, s
J	first curvature equal to twice the mean curvature
j	Jacobian
$\mathbf{j}$	fluid momentum
$K_{E\alpha}$	deviation kinetic energy per mass of entity α
$K_E^{\bar{\alpha}}$	entity-based macroscale deviation kinetic energy, $\langle (\mathbf{v}_\alpha - \mathbf{v}^{\bar{\alpha}}) \cdot (\mathbf{v}_\alpha - \mathbf{v}^{\bar{\alpha}})_{\Omega_\alpha, \Omega_\alpha, \rho_\alpha} \rangle / 2$
$\hat{k}^{wn}$	parameter for rate of relaxation of interfacial area

$\hat{k}_1^{wn}$ parameter for rate of relaxation of interfacial area
$\underset{\kappa\to\alpha}{\overset{M}{\kappa\to\alpha}}$ microscale transfer rate of mass of entity κ to entity α per entity extent
M macroscale transfer rate of mass of entity κ to entity α per entity extent
$\mathcal{M}_*^{\bar{\bar{\alpha}}}$ particular material derivative form of a macroscale entity mass conservation equation
$\mathbf{M}$ transformation matrix
$\mathbf{m}$ vector of moments obtained as a linear combination of the distributions $\mathbf{f}$
$\mathbf{n}_\alpha$ unit normal vector outward from boundary of entity α
ns interface between n and s phases
$\mathcal{P}_*^{\bar{\bar{\alpha}}}$ particular material derivative form of a macroscale entity momentum conservation equation
P pressure, interfacial tension, or common curvilinear tension based upon entity qualifier
p pressure
p^{wn} capillary pressure of the wn interface
$\underset{\kappa\to\alpha}{\overset{Q}{\kappa\to\alpha}}$ general macroscale transfer rate of energy from entity κ to entity α
Q general macroscale transfer rate of energy from entity κ to entity α
$\mathbf{q}$ nonadvective energy flux
$\mathbf{q}^{\bar{\bar{\alpha}}}$ macroscale nonadvective energy flux associated with entity α
R radius
$\hat{R}$ closure scalar
r general integration variable
$\mathcal{S}_*^{\bar{\bar{\alpha}}}$ particular material derivative form of a macroscale entity entropy balance
$s^{\bar{\bar{\alpha}}}$ saturation of fluid phase α
$\hat{\mathbf{S}}$ diagonal matrix of relaxation rates
T transport theorem
$\underset{\kappa\to\alpha}{\overset{\mathbf{T}}{\kappa\to\alpha}}$ general microscale transfer rate of momentum from entity κ to entity α
$\mathbf{T}$ general macroscale transfer rate of momentum from entity κ to entity α
$\mathcal{T}_*^{\bar{\bar{s}}}$ particular material derivative form of a macroscale Euler equation for a solid
$\mathcal{T}_*^{\bar{\bar{\alpha}}}$ particular material derivative form of a macroscale Euler equation for an entity
$\mathcal{T}_{\mathcal{G}*}^{\bar{\bar{s}}}$ particular macroscale form of the material derivative of the body source potential of a solid phase
$\mathcal{T}_{\mathcal{G}*}^{\bar{\bar{\alpha}}}$ particular macroscale form of the material derivative of the entity body source potential
t time
δt time step
$\mathbf{t}$ stress tensor
$\mathbf{t}^{\bar{\bar{\alpha}}}$ macroscale stress tensor for entity α
V set of variables
$\mathbf{v}$ velocity
$\mathbf{v}^{\alpha,\kappa}$ velocity of flow in an entity averaged over the boundary of the entity
W weighting function for averaging
w_{xx} free parameter in the MRT scheme
w_i weight for the LBM
w wetting phase
wn interface between w and n phases
wns common curve at boundary of wn, ws, and ns interfaces
ws interface between w and s phases
$\mathbf{w}$ velocity of a domain boundary
$\mathbf{w}_{wn}$ vector velocity of normal component of wn interface, $\mathbf{v}_{wn}\cdot\mathbf{n}_w\mathbf{n}_w$

$\mathbf{X}$	position vector in a solid in the initial state
$\mathcal{X}_k$	set of neighboring lattice sites to site $\mathbf{x}_k$
$\mathbf{x}$	position vector
$\delta_s\mathbb{Z}_d$	regular lattice space in d dimensions

Greek Symbols

α	entity index
β	entity index
Γ	boundary of a domain
γ	interfacial or surface tension; common curvilinear tension
ϵ	porosity
$\epsilon^{\bar{\bar{\alpha}}}$	specific entity measure, $\langle 1\rangle_{\Omega_\alpha,\Omega}$
ζ	parameter controlling interfacial width in LBM
η	entropy density
$\eta^{\bar{\bar{\alpha}}}$	macroscale entropy of entity α per volume, $\langle \eta_\alpha\rangle_{\Omega_\alpha,\Omega}$
θ	temperature
$\theta^{\bar{\bar{\alpha}}}$	entropy weighted macroscale temperature of entity α, $\langle \theta_\alpha\rangle_{\Omega_\alpha,\Omega_\alpha,\eta_\alpha}$
$\kappa_G^{\bar{\bar{=}}wns}$	macroscale geodesic curvature
$\kappa_N^{\bar{\bar{=}}wns}$	macroscale normal curvature
Λ	entropy production rate
$\Lambda^{\bar{\bar{\alpha}}}$	macroscale entropy production rate associated with entity α
μ	chemical potential
ρ	mass density
σ	LBM parameter used to control the interfacial tension
σ	solid-phase stress tensor
$\sigma^{\bar{\bar{s}}}$	macroscale solid-phase stress tensor
τ	dissipative part of the stress tensor
ϕ	dimensionless density field
ϕ_s	solid-phase value of dimensionless density field set to control contact angle
$\Phi_{\kappa\to\alpha}^{\bar{\bar{=}}}$	general macroscale transfer of entropy from entity κ to entity α
$\varphi^{\bar{\bar{=}}ws,wn}$	macroscale measure of contact angle
ϕ	nonadvective entropy flux
$\varphi^{\bar{\bar{\alpha}}}$	macroscale nonadvective entropy flux associated with entity α
$\phi_{ws,wn}$	microscale contact angle
$\chi_\alpha^{\bar{\bar{k}}}$	fraction of boundary of entity α in contact with entity κ, $\langle 1\rangle_{\Omega_\kappa,\Omega_\alpha}$
Ψ	body force potential density
$\Psi^{\bar{\bar{\alpha}}}$	entity-based macroscale body force potential density
ψ	body force potential per unit mass
$\psi^{\bar{\bar{=}}\alpha,\kappa}$	macroscale average of body force potential density associated with one entity averaged over a lower-dimensional entity
Ω	averaging domain
Ω_α	domain of entity α

Superscripts

eq	equilibrium value
n	macroscale nonwetting-phase qualifier
ns	macroscale qualifier for interface between n and s phases
ss	total surface of solid-phase qualifier

s	macroscale solid-phase qualifier
T	transpose
w	macroscale wetting-phase qualifier
wn	macroscale qualifier for interface between w and n phases
wns	macroscale qualifier for common curve where wn, ws, and ns interfaces meet
ws	macroscale qualifier for interface between w and s phases
α	macroscale entity qualifier
α	intrinsic average over entity α or macroscale property of entity α
$\overline{\alpha}$	mass average over entity α
$\overline{\overline{\alpha}}$	uniquely defined average over α
–	above a superscript refers to a density-weighted macroscale average
=	above a superscript refers to a uniquely defined macroscale average
$'$	vector tangent to a surface
$''$	vector tangent to a common curve

Subscripts

eq	equilibrium value
$\mathcal{E}$	associated with the total energy conservation equation
eq	equilibrium
$\mathcal{G}$	associated with the potential energy equation
$\mathcal{M}$	associated with the mass conservation equation
n	microscale nonwetting-phase qualifier
ns	microscale qualifier for interface between n and s phases
$\mathcal{P}$	associated with the momentum conservation equation
s	microscale solid-phase qualifier
ss	refers to the total boundary of the s phase
T	total
T	associated with the thermodynamic equation
$\mathcal{T}_{\mathcal{G}}$	associated with the derivative of potential energy equation
w	microscale wetting-phase qualifier
wn	microscale qualifier for interface between w and n phases
wns	microscale qualifier for common curve where wn, ws, and ns interfaces meet
ws	microscale qualifier for interface between w and s phases
α	microscale entity qualifier
$\alpha\alpha$	refers to the total boundary of entity α

Other Mathematical Symbols

$\mathrm{D}_\alpha/\mathrm{D}t$	material derivative with microscale velocity $\mathbf{v}_\alpha$
$\mathrm{D}^{\overline{\alpha}}/\mathrm{D}t$	material derivative with macroscale velocity $\mathbf{v}^{\overline{\alpha}}$
$\mathrm{D}'^{\overline{s}}/\mathrm{D}t$	material derivative on a surface where the macroscale solid is employed, $\partial'/\partial t + \mathbf{v}^{\overline{s}} \cdot \nabla'$
$\mathrm{D}''^{\overline{s}}/\mathrm{D}t$	material derivative on a curve where the macroscale solid is employed, $\partial''/\partial t + \mathbf{v}^{\overline{s}} \cdot \nabla''$
$\partial'/\partial t$	partial time derivative at a point fixed on a surface
$\partial''/\partial t$	partial time derivative at a point fixed on a common curve
$\partial^{(n)}/\partial t$	partial time derivative at a point fixed on 3 – n-dimensional entity, (n) is replaced by n primes
∇'	microscale surficial del operator
∇''	microscale common curve del operator
$\nabla^{(n)}$	microscale del operator for a 3 – n-dimensional entity where (n) is the number of primes
∇_X	gradient operator with respect to $\mathbf{X}$ coordinates

∇_x gradient operator with respect to macroscale **x** coordinates
(n) denotes the number of primes that should appear
$\hat{}$ a parameter defined at the scale indicated by the subscript or superscript on the parameter

$\langle f_\alpha \rangle_{\Omega_\beta,\Omega_\gamma,W} = \left(\int_{\Omega_\beta} W f_\alpha \, d\mathfrak{r} \right) \Big/ \left(\int_{\Omega_\gamma} W \, d\mathfrak{r} \right)$, general average of microscale property f_α

$f_\alpha^\beta = \langle f_\alpha \rangle_{\Omega_\beta,\Omega_\beta}$
$f^\alpha = \langle f_\alpha \rangle_{\Omega_\alpha,\Omega_\alpha}$, intrinsic average
$f_\alpha^{\bar{\beta}} = \langle f_\alpha \rangle_{\Omega_\beta,\Omega_\beta,\rho_\alpha}$, general density-weighted average
$f^{\bar{\alpha}} = \langle f_\alpha \rangle_{\Omega_\alpha,\Omega_\alpha,\rho_\alpha}$, intrinsic density-weighted average

Abbreviations

CIT	classical irreversible thermodynamics
DNP	disconnected nonwetting phase
LBM	lattice Boltzmann method
MRT	multirelaxation time
TCAT	thermodynamically constrained averaging theory

ACKNOWLEDGMENTS

This work was supported by National Science Foundation Grant 0941235, Department of Energy Grant DE-SC0002163, and Army Research Office Grant W911NF-14-1-0287.

REFERENCES

1. B. Ahrenholz, J. Toelke, P. Lehmann, A. Peters, A. Kaestner, M. Krafczyk, and W. Durner. Prediction of capillary hysteresis in a porous material using lattice-Boltzmann methods and comparison to experimental data and a morphological pore network model. *Advances in Water Resources*, 31(9):1151–1173, 2008.
2. R. I. Al-Raoush and C. S. Wilson. Extraction of physically realistic pore network properties from three-dimensional synchrotron x-ray microtomography images of unconsolidated porous media systems. *Journal of Hydrology*, 300(1–4):44–64, 2005.
3. T. B. Anderson and R. Jackson. A fluid mechanical description of fluidized beds. *Industrial and Engineering Chemistry Fundamentals*, 6:527–539, 1967.
4. Y. Bachmat. Spatial macroscopization of processes in heterogeneous systems. *Israel Journal of Technology*, 10:391–403, 1972.
5. M. Bailyn. *A Survey of Thermodynamics*. American Institute of Physics Press, New York, 1994.
6. J. Bear. *Hydraulics of Groundwater*. McGraw-Hill, New York, 1979.
7. L. S. Bennethum and J. H. Cushman. Multiphase, multicomponent theory for multiscale swelling systems with interfaces. Part II: Constitutive theory. *International Journal of Engineering Science*, 34(2):147–169, 1996.
8. H. Bertin, M. Quintard, and V. Corpel. Two-phase flow in heterogeneous porous media III: Laboratory experiments for flow parallel to a stratified system. *Transport in Porous Media*, 5(6):543–590, 1990.
9. P. Bobeck. *The Public Fountains of the City of Dijon* (translation of *Les Fontaines Publiques de la Ville de Dijon by Henry Darcy, 1856*). Geotechnical Translations, Austin, TX, 2004.
10. M. M. Britton. Porous media studied by MRI. *eMagRes*, 2011.
11. H. B. Callen. *Thermodynamics and an Introduction to Thermostatistics*. Wiley, New York, 1985.
12. J. T. Cheng. Fluid flow in ultrafine structures. Master's thesis, Purdue University, West Lafayette, IN, 2002.
13. J. T. Cheng, L. J. Pyrak-Nolte, D. D. Nolte, and N. J. Giordano. Linking pressure and saturation through interfacial areas in porous media. *Geophysical Research Letters*, 31(8), 2004.
14. V. Cnudde and M. N. Boone. High-resolution x-ray computed tomography in geosciences: A review of the current technology and applications. *Earth–Science Reviews*, 123:1–17, 2013.

15. G. H. Crapiste, E. Rotstein, and S. Whitaker. A general closure scheme for the method of volume averaging. *Chemical Engineering Science*, 41:227–235, 1986.
16. H. Darcy. *Les Fontaines Publiques de la Ville de Dijon*. Dalmont, Paris, France, 1856.
17. H. Darcy. Determination of the laws of flow of water through sand. In R. A. Freeze and W. Back, eds., *Physical Hydrology*. Hutchinson Ross, Stroudsburg, PA, 1983.
18. K. G. Denbigh. *The Principles of Chemical Equilibrium*. Cambridge University Press, Cambridge, U.K., 1981.
19. D. d'Humiéres, I. Ginzburg, M. Krafczyk, P. Lallemand, and L. S. Luo. Multiple-relaxation-time lattice Boltzmann models in three dimensions. *Philosophical Transactions of the Royal Society of London Series A: Mathematical Physical and Engineering Sciences*, 360:437–451, 2002.
20. A. L. Dye, J. E. McClure, C. T. Miller, and W. G. Gray. Description of non-darcy flows in porous medium systems. *Physical Review E*, 87(3), 2013.
21. F. Golfier, B. D. Wood, L. Orgogozo, M. Quintard, and M. Bués. Biofilms in porous media: Development of macroscopic transport equations via volume averaging with closure for local mass equilibrium conditions. *Advances in Water Resources*, 463–485(32):3, 2009.
22. W. G. Gray and S. M. Hassanizadeh. Averaging theorems and averaged equations for transport of interface properties in multiphase systems. *International Journal of Multiphase Flow*, 15(1):81–95, 1989.
23. W. G. Gray and P. C. Y. Lee. On the theorems for local volume averaging of multiphase systems. *International Journal of Multiphase Flow*, 3:333–340, 1977.
24. W. G. Gray and C. T. Miller. Thermodynamically constrained averaging theory approach for modeling flow and transport phenomena in porous medium systems: 1. Motivation and overview. *Advances in Water Resources*, 28(2):161–180, 2005.
25. W. G. Gray and C. T. Miller. Thermodynamically constrained averaging theory approach for modeling flow and transport phenomena in porous medium systems: 5. Single-fluid-phase transport. *Advances in Water Resources*, 32(5):681–711, 2009.
26. W. G. Gray and C. T. Miller. Thermodynamically constrained averaging theory approach for modeling flow and transport phenomena in porous medium systems: 8. Interface and common curve dynamics. *Advances in Water Resources*, 33(12):1427–1443, 2010.
27. W. G. Gray and C. T. Miller. A generalization of averaging theorems for porous medium analysis. *Advances in Water Resources*, 62, 227–237, 2013.
28. W. G. Gray and C. T. Miller. *Introduction to the Thermodynamically Constrained Averaging Theory for Porous Medium Systems*. Advances in Geophysical and Environmental Mechanics and Mathematics (AGEM^2). Springer, Cham, Switzerland, 2014.
29. W. G. Gray and K. O'Neill. On the development of Darcy's law for the general equations for flow in porous media. *Water Resources Research*, 12(2):148–154, 1976.
30. W. G. Gray, A. Leijnse, R. L. Kolar, and C. A. Blain. *Mathematical Tools for Changing Spatial Scales in the Analysis of Physical Systems*. CRC Press, Boca Raton, FL, 1993.
31. W. G. Gray, A. F. B. Tompson, and W. E. Soll. Closure conditions for two-fluid flow in porous media. *Transport in Porous Media*, 47(1):29–65, 2002.
32. Z. Guo and T. S. Zhao. Lattice Boltzmann model for incompressible flows through porous media. *Physical Review E*, 66:036304-1–036304-9, 2002.
33. S. M. Hassanizadeh and W. G. Gray. General conservation equations for multi-phase systems: 1. Averaging procedure. *Advances in Water Resources*, 2(3):131–144, 1979.
34. S. M. Hassanizadeh and W. G. Gray. Toward an improved description of the physics of two-phase flow. *Advances in Water Resources*, 16(1):53–67, 1993.
35. X. He and L. S. Luo. A priori derivation of the lattice Boltzmann equation. *Physical Review E*, 55:R6333–R6336, 1997.
36. M. Hilpert, J. F. McBride, and C. T. Miller. Pore-scale modeling of hysteretic flow in porous media. In *Sixth SIAM Conference on Mathematical and Computational Issues in the Geosciences*, Boulder, CO, 2001.
37. F. A. Howes and S. Whitaker. The spatial averaging theorem revisited. *Chemical Engineering Science*, 40:1387–1392, 1985.
38. H. Huang, D. T. J. Thorne, M. G. Schaap, and M. C. Sukop. Proposed approximation for contact angles in Shan-and-Chen-type multicomponent multiphase lattice Boltzmann models. *Physical Review E*, 76(6, Part 2), 2007.
39. A. B. S. Jackson, C. T. Miller, and W. G. Gray. Thermodynamically constrained averaging theory approach for modeling flow and transport phenomena in porous medium systems: 6. Two-fluid-phase flow. *Advances in Water Resources*, 32(6):779–795, 2009.

40. L. F. Konikow and P. D. Glynn. Modeling groundwater flow and quality. In *Essentials of Medical Geology*, pp. 727–753. Springer, Netherlands, 2013.
41. M. Latva-Kokko and D. Rothman. Static contact angle in lattice Boltzmann models of immiscible fluids. *Physical Review E*, 72(4, Part 2), 2005.
42. G. Lebon, D. Jou, and J. Casas-Vázquez. *Understanding Nonequilibrium Thermodynamics*. Springer, Berlin, Germany, 2008.
43. C. Marle. Ècoulements monophasiques en milieu poreux. *Revue de L'Institut Français du Pétrole*, 22(10):1471–1509, 1967.
44. G. A. Maugin. *The Thermomechanics of Nonlinear Irreversible Behaviors: An Introduction*. World Scientific Press, Singapore, 1999.
45. J. E. McClure, D. Adalsteinsson, C. Pan, W. G. Gray, and C. T. Miller. Approximation of interfacial properties in multiphase porous medium systems. *Advances in Water Resources*, 30(3):354–365, 2007.
46. J. E. McClure, J. F. Prins, and C. T. Miller. A novel heterogeneous algorithm to simulate multiphase flow in porous media on multicore CPU-GPU systems. *Computer Physics Communication*, 185:1865–1874, 2014.
47. C. T. Miller and W. G. Gray. Thermodynamically constrained averaging theory approach for modeling flow and transport phenomena in porous medium systems: 2. Foundation. *Advances in Water Resources*, 28(2):181–202, 2005.
48. C. T. Miller, G. Christakos, P. T. Imhoff, J. F. McBride, J. A. Pedit, and J. A. Trangenstein. Multiphase flow and transport modeling in heterogeneous porous media: Challenges and approaches. *Advances in Water Resources*, 21(2):77–120, 1998.
49. N. R. Morrow. Irreducible wetting-phase saturations in porous media. *Chemical Engineering Science*, 25:1799–1815, 1970.
50. J. Niessner and S. M. Hassanizadeh. A model for two-phase flow in porous media including fluid-fluid interfacial area. *Water Resources Research*, 44(W08439), 2008.
51. J. Niessner, S. Berg, and S. M. Hassanizadeh. Comparison of two-phase Darcy's Law with a thermodynamically consistent approach. *Transport in Porous Media*, 88:133–148, 2011.
52. C. Pan, L.-S. Luo, and C. T. Miller. An evaluation of lattice Boltzmann schemes for porous medium flow simulation. *Computers & Fluids*, 35(8–9):898–909, 2006.
53. D. Pavone. A Darcy's law extension and a new capillary pressure equation for two-phase flow in porous media. In *Proceedings of the 65th Annual Technical Conference of the Society of Petroleum Engineers*, volume Rep. SPE 20474, pp. 111–119, New Orleans, LA, 1990. Society of Petroleum Engineers.
54. M. Quintard and S. Whitaker. Two-phase flow in heterogeneous porous media: The method of large-scale averaging. *Transport in Porous Media*, 3(4):357–413, 1988.
55. M. Quintard and S. Whitaker. Transport in chemically and mechanically heterogeneous porous media. I: Theoretical development of region-averaged equations for slightly compressible single-phase flow. *Advances in Water Resources*, 19(1):29–47, 1996.
56. M. Quintard and S. Whitaker. Theoretical analysis of transport in porous media. In K. Vafai, ed., *Handbook of Porous Media*, pp. 1–52. Marcel Dekker, New York, 2000.
57. N. R. Rossman and V. A. Zlotnik. Review: Regional groundwater flow modeling in heavily irrigated basins of selected states in the western United States. *Hydrogeology Journal*, 21:1173–1192, September 2013.
58. T. Sakaki, D. M. O'Carroll, and T. H. Illangasekare. Direct quantification of dynamic effects in capillary pressure for drainage-wetting cycles. *Vadose Zone Journal*, 9:424–437, 2010.
59. G. Segol. 1994. *Classic Groundwater Simulations*: *Proving and Improving Numerical Models*. Englewood Cliffs, N.J.: Prentice Hall.
60. J. C. Slattery. Flow of viscoelastic fluids through porous media. *American Institute of Chemical Engineers Journal*, 13(6):1066–1071, 1967.
61. J. C. Slattery. *Advanced Transport Phenomena*. Cambridge University Press, Cambridge, U.K., 1999.
62. P. Spanne, J. F. Thovert, C. J. Jacquin, W. B. Lindquist, K. W. Jones, and P. M. Adler. Synchrotron computed microtomography of porous-media—Topology and transports. *Physical Review Letters*, 73(14):2001–2004, 1994.
63. G. L. Stegemeier. Mechanism of entrapment and mobilization of oil in porous media. In *AIChE Symposium on Improved Oil Recovery by Surfactant and Polymer Flooding*, pp. 55–91. Academic Press Inc., New York, 1977.
64. P. W. Takhar. Unsaturated fluid transport in swelling poroviscoelastic biopolymers. *Chemical Engineering Science*, 109:98–110, 2014.

65. L. Talon, D. Bauer, N. Gland, S. Youssef, H. Auradou, and I. Ginzburg. Assessment of the two relaxation time lattice-Boltzmann scheme to simulate Stokes flow in porous media. *Water Resources Research*, 48, 2012.
66. I. Vavruch. Conceptual problems of modern irreversible thermodynamics. *Chemicke Listy*, 96(5):271–275, 2002.
67. S. Whitaker. Diffusion and dispersion in porous media. *American Institute of Chemical Engineers Journal*, 13(3):420–427, 1967.
68. S. Whitaker. Advances in theory of fluid motion in porous media. *Industrial and Engineering Chemistry*, 61(12):14–28, 1969.
69. S. Whitaker. *The Method of Volume Averaging*. Kluwer Academic Publishers, Dordrecht, the Netherlands, 1999.
70. D. Wildenschild and A. P. Sheppard. X-ray imaging and analysis techniques for quantifying pore-scale structure and processes in subsurface porous medium systems. *Advances in Water Resources*, 51:217–246, 2013.
71. B. D. Wood, F. Cherblanc, M. Quintard, and S. Whitaker. Volume averaging for determining the effective dispersion tensor: Closure using periodic unit cells and comparison with ensemble averaging. *Water Resources Research*, 39(8), August 2003.